AlCrN HARD COATINGS DEPOSITED BY MAGNETRON SPUTTERING – SCRATCH, WEAR AND CREEP BEHAVIOR

BY
SHAHNAWAZ ALAM

A Thesis Presented to the
DEANSHIP OF GRADUATE STUDIES

KING FAHD UNIVERSITY OF PETROLEUM & MINERALS

DHAHRAN, SAUDI ARABIA

In Partial Fulfillment of the
Requirements for the Degree of

MASTER OF SCIENCE

In

MECHANICAL ENGINEERING

APRIL 2013

KING FAHD UNIVERSITY OF PETROLEUM & MINERALS
DHAHRAN- 31261, SAUDI ARABIA
DEANSHIP OF GRADUATE STUDIES

This thesis, written by **Shahnawaz Alam** under the direction his thesis advisor and approved by his thesis committee, has been presented and accepted by the Dean of Graduate Studies, in partial fulfillment of the requirements for the degree of **MASTER OF SCIENCE IN MECHANICAL ENGINEERING.**

Dr. Zuhair Mattoug Gasem
Advisor

Dr. Zuhair Mattoug Gasem
Department Chairman

Dr. Tahar Laoui
Member

Dr. Syed Fida Hassan
Member

Dr. Salam A. Zummo
Dean of Graduate Studies

5/6/13

Date

Dedicated to my Mother, Father, Brothers and Sisters

Whose constant prayers and inspiration led to

this wonderful accomplishment

ACKNOWLEDGMENTS

All praises to Allah (SWT) for His blessing and guidance on me. May the peace and blessings of Allah (SWT) be upon His dearest prophet, Muhammad (peace be upon him).

I express my sincere gratitude to King Fahd University of Petroleum & Minerals, Saudi Arabia, for providing an opportunity to me to pursue Master of Science in Mechanical Engineering, and providing the support for my studies and research work.

I would like to express my sincere appreciation and gratitude to my thesis advisor, Dr. Zuhair Mattoug Gasem, who has always helped me in technical, social, ethical and financial support throughout my thesis, especially his guidance and cooperation in supervising this thesis work. I express my thankfulness for Dr. Syed Fida Hassan for his contribution and support throughout my KFUPM life. I wish to thank Dr. Tahar Laoui for his support in my work. I am grateful to the previous chairman of the Mechanical Engineering Department, Dr. Amro Qutub for his help and cooperation. I am also thankful to Mr Latif Hashmi for his help in my experimental work.

I am grateful to the faculty members of the Mechanical Engineering Department for the knowledge that they bestowed upon me, and for their kind help. I am thankful to all staffs and technicians who helped me a lot during work, Special thanks to Mr. Safdar Hussain, Mr. Sarfaraz Ahmad Furqan, Mr. Mirza Murtuza Ali Baig for their help and services during the course of this thesis. I thank to all my colleagues and friends, especially to my best friend ever Mr. Zeeshan Alam, for their support.

Finally, I offer my sincere thanks to my parents, my brothers and sisters, for enduring my long stay away from home, and the inspirations and support throughout.

TABLE OF CONTENTS

LIST OF TABLES

LIST OF FIGURES

ABSTRACT

Full Name	:	SHAHNAWAZ ALAM
Thesis Title	:	AlCrN HARD COATING DEPOSITED BY MAGNETRON SPUTTERING- SCRATCH, WEAR AND CREEP BEHAVIOR.
Major Field	:	MECHANICAL ENGINEERING
Date of Degree	:	APRIL 2013

Nitride based hard coatings find increasing applications in the tool industry. Ternary nitride coating systems generally display excellent performance. Aluminium Chromium Nitride (AlCrN) films are probably the most promising coatings for high temperature applications due to their excellent oxidation resistance.

AlCrN coatings were deposited on tool steel substrates by magnetron sputtering method. Cr/Al composition ratio in the coating was varied by using an aluminum target plate with 4 and 8 chromium plugs. Two coating compositions have been considered for this study with Cr/Al of approximately 2.0 and 0.8. The coatings were deposited using three biasing voltages of -30 V, -50 V, and -60 V.

The effects of Cr/Al ratio and biasing voltage on the scratch resistance, wear resistance and creep resistance were analyzed. The coating compositions, surface morphologies, cross-sectional composition variations, phases and vicker hardnesses were characterized. Results showed that all the coatings were comprised of multiple layers with varying composition. An interface layer of around 500 nm was observed between the substrate and the coatings. The scratch resistance was higher for the coating with higher Cr/Al content. Biasing voltage exhibited no clear correlation with the coating critical load. Coating delamination was found in higher Cr/Al content coating with no observable coating delamination in lower Cr/Al coating. The wear rate decreased with increasing biasing voltage for fixed Cr/Al content probably because of increased hardness. Comparable wear rates were obtained for Cr/Al content of 2.0 and 0.8 at a fixed biasing

voltage. This may be because of no coating delamination in lower Cr/Al content coating. The creep resistance of AlCrN based coatings was sensitive to Cr/Al content. At low temperatures (i.e. 25 ^{o}C, 50 ^{o}C and 75 ^{o}C), creep resistance was higher for the high Cr/Al coating. At 100 ^{o}C, indenter penetration reached up to 60 % of the coating thickness. The large indenter penetration invalidated the creep results at 100 ^{o}C.

ملخص الرسالة

سلوك الخدش والتاكل والزحف لطلاء الألومنيوم كروم نيتريد الصلد المترسب بطريقة الرش المغناطيسية

الطلاء الصلد المحتوى على النيتريد له تطبيقات متزايدة فى صناعة ادوات القطع . انظمة الطلاء ثلاثى النيتريد اظهرت اداء افضل . طلاءات الألومنيوم كروم نيتريد قد يكون الطلاء الافضل للتطبيقات عالية الحرارة ويرجع ذلك الى مقاومته الممتازة للتاكسد.

تم طلاء الألومنيوم كروم نيتريد على قوام اداة قطع مصنعة من الصلب بطريقة الرش المغناطيسية . تم تغيير نسبة الكروم الى الالومينيوم فى الطلاء باستخدام لوح الومينيوم مع مقابس كروم 2 و0.8. تم استخدام طلاء بتركيبين مختلفين فى هذه الدراسه بنسبة كروم الى الالومينيوم 2 الى 0.8 . وتم ترسيب الطلاء باستخدام جهد -30,-50,-60 فولت .

تم دراسة تاثير كلا من نسبة الكروم الى الالومينيوم و الفولت على مقاومة الخدش والبرى والزحف. وتم قياس مكونات الطلاء و تغيرمورفولوحيا السطح وتغيير التركيب فى مساحة المقطع وكذلك قياس الصلادة

اوضحت النتائج ان كل الطلاءات تتكون من طبقات متعددة يتركيبات متنوعة . وايضا وجود طبقة مشتركة بسمك 500 نانوميتر بين الطلاء والركيزة . واوضحت النتائج ان مقاومة الخدش كانت عالية فى الطلاء دات نسبة عاليه من الكروم للالومينيوم. وكذلك اظهرت النتائج عدم وجود علاقة واصحة بين الجهد والحمل الحرج للطلاء,ولوحظ وجود تنسل فى الطلاء المكون من نسبة عاليه من الكروم للالومينيوم وعدم ظهوره فى الطلاء المكون من نسب منخفضه من الكروم للالومينيوم.

معدل التاكل يقل بزيادة الجهد مع ثبات نسبة الكروم للالومينيوم نتيجة زيادة الصلاده . اظهرت النتائج النتائج وجود تباين فى مقاومة البرى لنسب 2 و0.8 من الكروم للالومينيوم مع ثبات الجهد , ربما يرجع ذلك لعدم تنسل الطلاء المكون من نسب منخفضه من الكروم للالومينيوم. مقاومة الزحف للطلاء المحتوى على الألومنيوم كروم نيتريد وجد انها تتاثر بنسبة الكروم للالومينيوم . وكانت مقاومة الزحف عالية عند درجات الحرارة المنخفضة (, 75,50,25) درجة مئويه فى الطلاء المكون من نسبة عاليه من الكروم للالومينيوم بينما عند درجة حرارة 100 درجة مئويه وصل تغلغل الجسم المحدث للاثر الى 60 % من سمك الطلاء مما حد من قيمة القياسات عند هذه الدرجة.

.

CHAPTER 1

INTRODUCTION

Materials highly resistant to wear, abrasion, erosion and corrosion are of utmost importance in many different industrial fields. It has led in the recent years to the development of coated components. In the sequence of coating several binary hard ceramic coating like TiN, AlN and CrN have been commercialized. The PVD nitride coatings with good oxidation, anti-corrosive and anti-adhesive properties, have found a wide industrial application as protective coatings for varied tools [1]. To further improve these properties of coatings, alloying with another metal to form a ternary hard coating has been explored. Various ternary nitride films such as Ti–Zr–N [2], Cr–Al–N [3] and Zr–Al–N [4] were developed.

The Al-Cr–N coatings are of high interest for tool and component applications, and probably the most promising nitrides for protective coatings [5]. Recently titanium-based coatings were replaced with Al-Cr-N layers because of their higher thermal stability and hardness, particularly in intermediate and high-speed cutting applications. Al-Cr-N provides high hardness, superior oxidation resistance and good tribological behavior [6].

1.1 Physical Vapor Deposition (PVD)

As the name suggest physical vapor deposition (PVD) technique is a vacuum deposition technique. In PVD method atoms are deposited from one surface to another surface physically. The coating method involves purely physical processes such as high temperature vacuum evaporation with subsequent condensation, or plasma sputter bombardment rather than involving a chemical reaction at the surface to be coated as in chemical vapor deposition.

Many methods are evolved and used to deposit thin film coating by incorporating the concept of physical vapor deposition (PVD) technique. Most commonly used methods are –

- Cathodic Arc Deposition or Arc ion deposition or Arc Ion Plating
- Electron Beam Physical Vapor Deposition
- Evaporative Deposition
- Pulsed Laser deposition
- Sputter Deposition

1.2 Magnetron Sputtering Process

Sputtering is the ejection of the atoms from one material (target) and depositing it on another surface (substrate). Ejections of atoms are done by means of ionized argon gas called as plasma. Process efficiency depends on the argon ion generation and their collision with the target. Magnetron sputtering is a improved sputtering process. In late 1970s efficiency of the sputtering process was improved by introducing permanent magnet [7]. However it was the development of the unbalanced magnetron sputtering process [8]. It incorporated closed field unbalanced magnetron sputtering up to early 1990s. Conventional magnetron sputtering process and unbalanced magnetron sputtering process differ very slightly but the difference in performance between these two magnetron processes is very significant. In an unbalanced magnetron all the field lines are closed between the central and outer poles in the magnetron, but some are directed towards the substrate, and some secondary electrons are able to follow these field lines. Consequently, the plasma is no longer strongly confined to the target region, but is also allowed to flow out towards the substrate. Schematic of balanced and unbalanced magnetron sputtering process is shown in Figure 1-1 [9].

There has been extensive work done to improve the coating process. In 1987, Danroc et al. [10] deposited the TiN coating by magnetron sputtering process. They studied the effect pumping speed and effect of inlet gas position. Apparatus used for their study is shown in Figure 1-2 [10]. They concluded that gas flow rate can lead to stability and reproducibility of the phenomena. In 1992, Lehan et al., studied the optical properties of aluminum oxide films at an order of magnitude higher deposition rate than conventional reactive magnetron sputtering. They observed that coatings deposited at a reduced pressure (0.27 Pa) produced dense, water-free coatings without compromising optical quality or deposition rate [11]. In the 90s tremendous research was carried on many aspects of coating processes. In 1992, Tsiogas et al. [12] presented a steady-state model for the reactive sputtering process. In this sequence, Werner et al. deposited decorative coating by using ZrB_{12} target and neon, argon and krypton as a process gas. They found that ZrB_{12} target produced a very fine and good corrosion resistant coating [13]. Sputtered nitride coatings were observed as potential capabilities to improve the tool life [14]. Nitiride based coatings were emphasized as hard coating. In 1996, M. Stüber deposited a metastable thin film material from Ti-B-C-N system by using magnetron sputtering process in different Ar + N_2 environments. They reported that new single phase crystal Ti-B-C-N provided very good tribological properties [15]. Apart from tribological properties other properties were also improved. In 1998, R. Manaila reported that TiN and $Ti_{1-x}Al_xN$ hard coating deposited by magnetron sputtering process were NaCl-type lattice [16]. L. Cunha studied the corrosion properties of TiN, (TiAl)N and CrN hard coatings deposited by magnetron sputtering process. They concluded that corrosion resistance depended on grains sizes and fine grain coating showed best corrosion resistance [17].

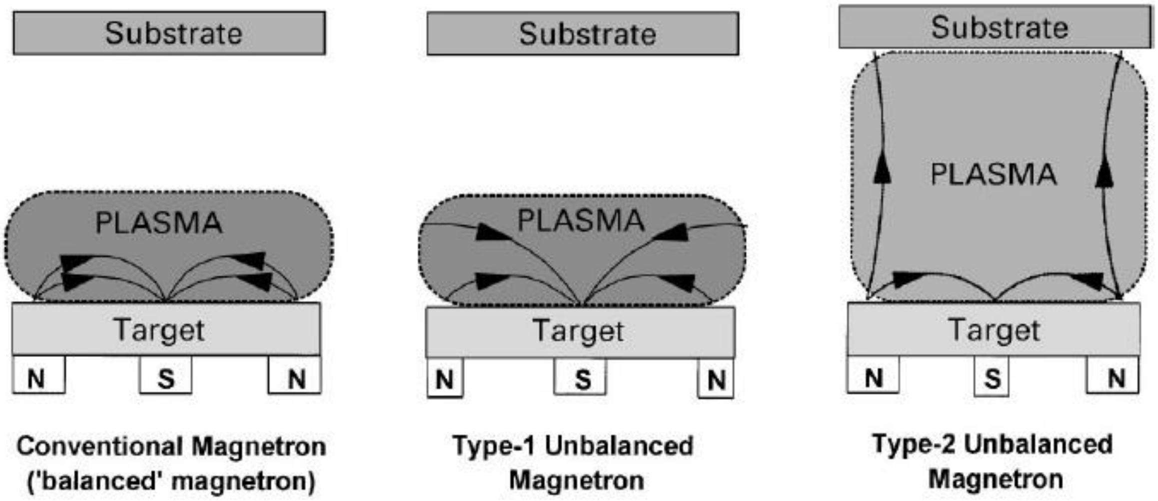

Figure 1-1 Schematic representation of the plasma confinement observed in conventional and unbalanced magnetrons [9].

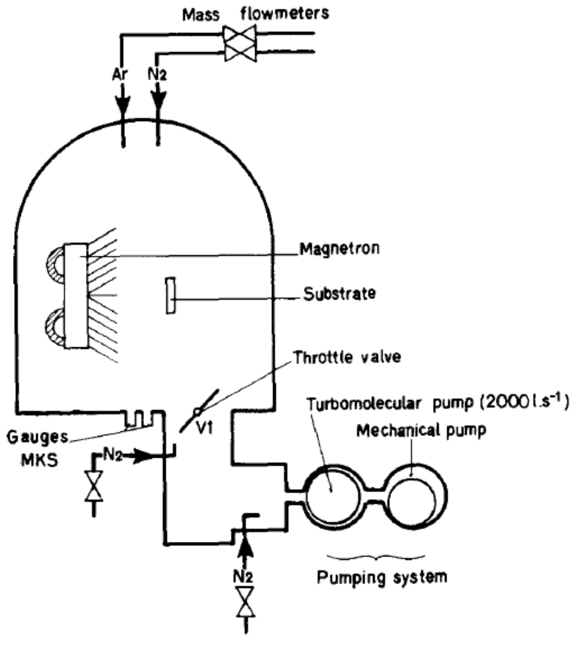

Figure 1-2 Schematic diagram of an early sputtering apparatus [10].

Improvement in the magnetron sputtering process was carried out by studying the parameters involved by depositing different types of coatings. In 2000, A. Lousa et. al. deposited BCN thin film near the B_4N composition by magnetron sputtering process. They studied the effect of N_2/Ar composition during coating. Effect of N_2/Ar composition on growth rate is shown in Figure 1-3. They reported that 2% N_2/Ar is the optimum plasma gas composition from the point of view of practical application [18]. In next year, Berlind [19] deposited Si-C-N thin film by using C and Si target in a mixed Ar/N_2 discharge. Schematic of substrate target arrangement is shown in Figure 1-4. Now magnetron sputtering is considered to be the most favorable deposition method on industrial level as it offers safety advantages, avoids the use of toxic gases and has low cost. Some protective coatings like TiN are produced by magnetron sputtering process on industrial scale. Recently used coating machines provide more control and good coating properties.

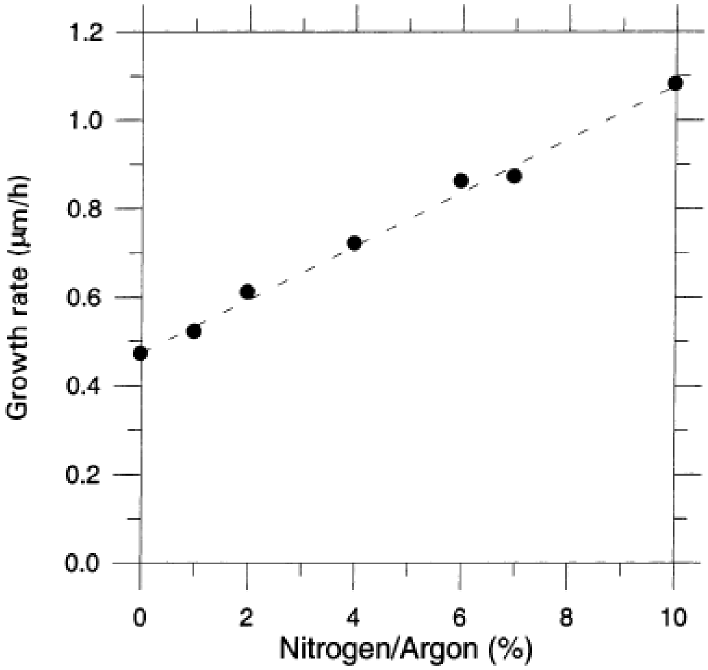

Figure 1-3 Dependence of BCN film growth rate on nitrogen/argon plasma gas composition [18].

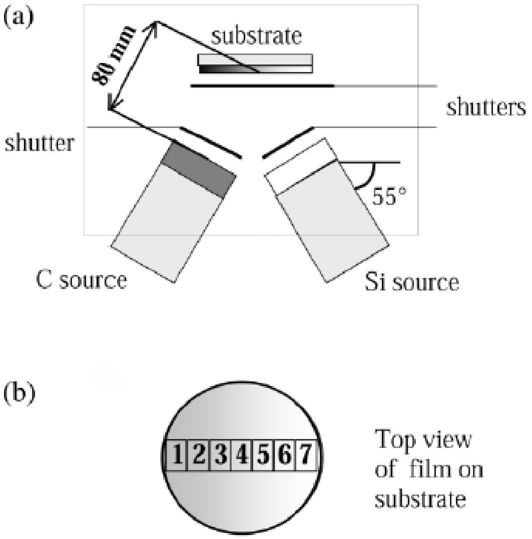

Figure 1-4 (a) Schematic view of the substrate-target geometry for co-sputter deposition, and (b) sample positions on the substrate with position 1 facing the C source and position 7 facing the Si source [19].

Schematic of magnetron sputtering process used by Song [20] in 2008 is shown in Figure 1-5. He prepared Aluminium-doped zinc oxide (ZnO:Al) films at different radio frequency powers. He found that the film growth rate was increased with increasing power. A graph plotted by his study is shown in Figure 1-6. For improvement in the coating properties several rotating magnetron sputtering processes were developed. Generally rotating type magnetron sputtering system provide multilayered coating and different target can be used in signal coating. Most recent used rotating magnetron sputtering setup is shown in Figure 1-7 [21].

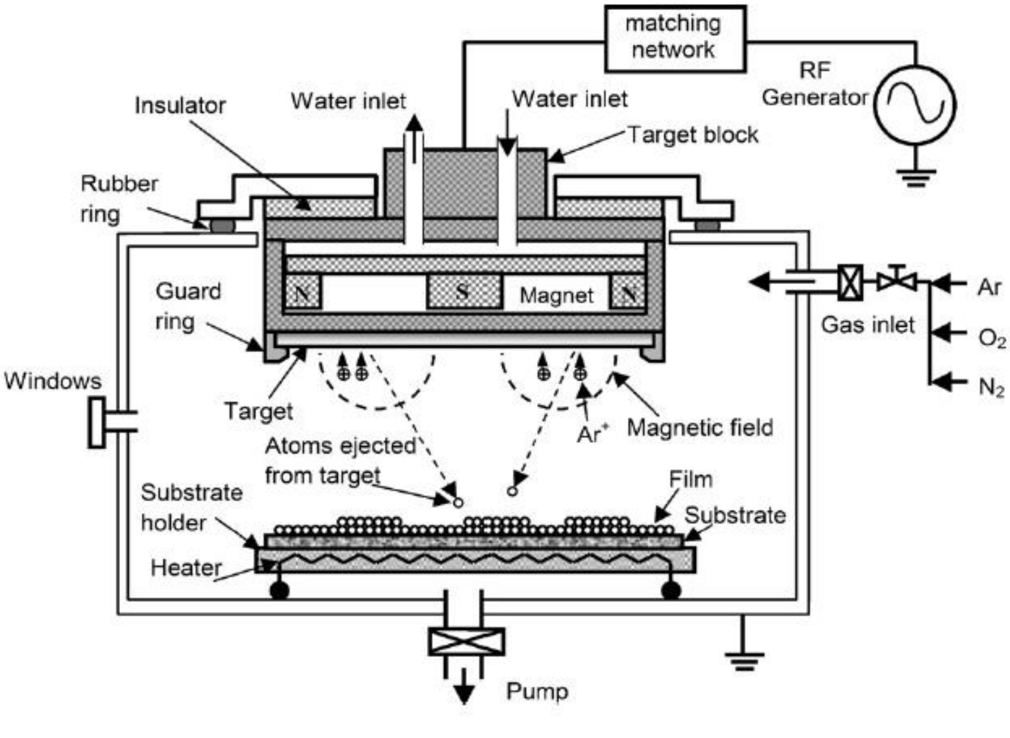

Figure 1-5 Schematic diagram of magnetron sputtering system used by song [20].

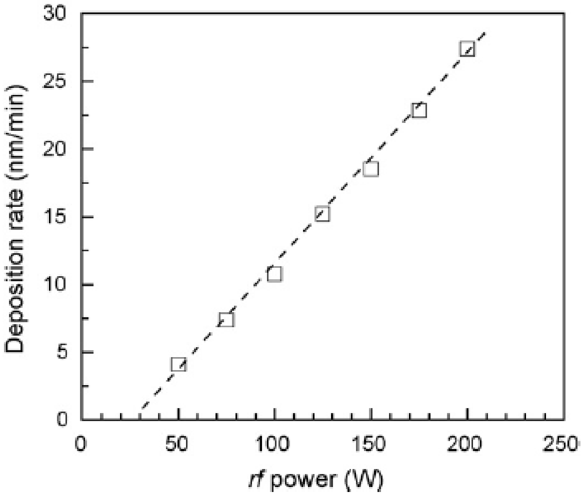

Figure 1-6 Deposition rate graph as function of radio frequency power obtained by D. Song [20].

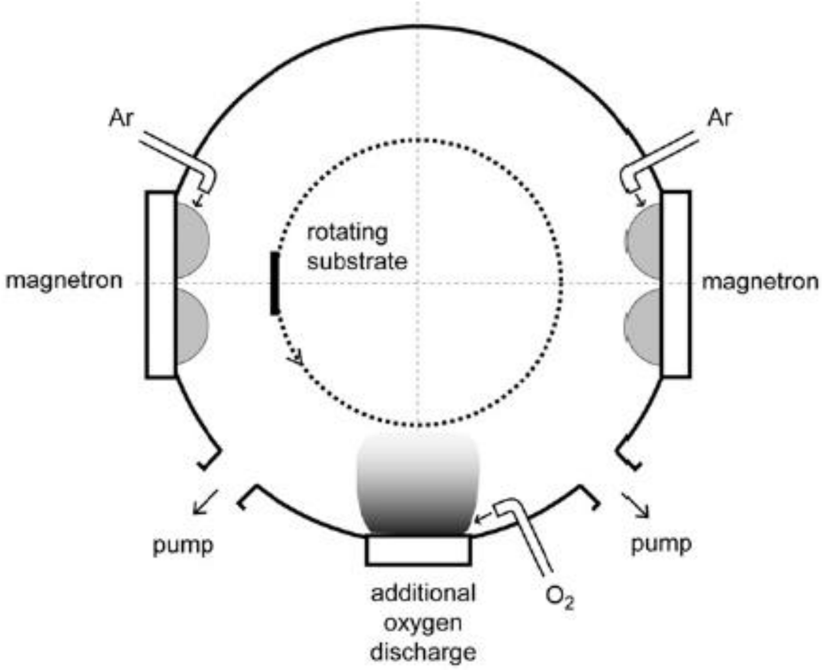

Figure 1-7 Schematic illustration of deposition device used for interrupted reactive sputtering process of transparent oxide films with additional oxygen discharge. Substrate is rotating and oxygen discharge is separated from one or more magnetron discharges by efficient pumping units. This process is patented as the MetaMode^{TM} process [21].

1.3 Objectives

The aim of the present study is to investigate the effects of Cr/Al content and biasing voltage on the properties of AlCrN coatings produced by magnetron sputtering process. Cr/Al ratio was varied by varying the target composition. The target was biased at different voltages. Target composition and biasing voltage are two very critical variables in deposition process. In general the target composition controls the coating material composition and biasing voltage affects its growth rates.

CHAPTER 2

LITERATURE REVIEW

This chapter gives an overview of the magnetron sputtering coating deposition process, coating materials, coating evaluation techniques and their corresponding behavior.

2.1 AlCrN Coating

Nitride based hard coatings became most versatile coating due to high hardness values and good tribological properties. High hardness, excellent wear and corrosion resistance enable them to improve tool life greatly [1, 22, 23]. Binary transition metal nitride films have been used widely as protective and wear resistant hard coatings for cutting and forming tools due to their superior mechanical and tribological properties [24]. However binary transition coatings do not pass in all conditions like high temperature [25], to overcome this problem a ternary nitride coating system was explored.

AlCrN is one of the most promising coatings for high temperature applications, due to their excellent oxidation resistance compared to other coatings. There has been extensive attention given in the deposition of AlCrN coating and its characterization. Hardness along with residual stresses obtained in literature is shown in Table 2-1 [26].

Table 2-1 Hardness and residual stresses values of AlCrN coatings reported in literature [26].

Authors	**Deposition mode**	**Substrate**	**Stress measurement**	**Stoichiometry**	**Thickness (μm)**	**Hardness, (GPa)**	**Residual stresses, (GPa)**
Hoy et al.[27]	Plasma PVD (Hauzer HC 750)	Steel substrate	Wafer curvature	$CrN_{0.65}$	1–3	30	0 to − 1.6
Reiter et al.[28]	Reactive cathodic arcprocess (Balzers RCSa)	Cemented carbide inserts	Three point bending	$Al_{0.21}Cr_{0.79}N$	4.8	31	− 2.46
				$Al_{0.46}Cr_{0.54}N$	4.8	39.1	− 4.89
				$Al_{0.71}Cr_{0.29}N$	4.7	38.5	− 3.49
				$Al_{0.83}Cr_{0.17}N$	5.7	21.2	− 1.86
				AlN	5	29.5	− 1.16
Endrino et al.[6]	Cathodic arc ion-plating mode (Balzers RCSa)	Cemented carbides		$Al_{0.7}Cr_{0.38}N$	3.5 ± 0.2	31.2 ± 6.2	
Kim and Lee[29]	Magnetron CFUBMS	Si (100) Nitrided AISI H13	Wafer curvature	$Al_{0.71}Cr_{0.29}N_{1.2}$		40.8	− 5.64
				$Al_{0.59}Cr_{0.41}N_{1.18}$		38	
				$Al_{0.5}Cr_{0.5}N_{1.2}$		36.5	− 5.36
				$Al_{0.44}Cr_{0.56}N_{1.2}$		33.8	
				$Al_{0.38}Cr_{0.62}N_{1.16}$		31.8	
				$Al_{0.31}Cr_{0.69}N_{1.1}$		30.5	− 4.5
				$AlN_{1.3}$		22.9	− 1.7
Fox-Rabinovich et al.[30]	Commercial	H1P cemented carbide inserts		$Al_{0.31}Cr_{0.69}N_{1.1}$	∼ 3.5	31	
Lin et al.[31]	Commercial	Cemented carbide inserts		BALINIT Alcrona		$HV_{0.05} = 3.2$	− 3

2.1.1 Thermal Stability

Thermal stability of the coating is important property especially when exposed to high temperature. Banakh et al. [3] deposited AlCrN nitride coating by magnetron sputtering process using Cr and Al targets in a mixed Ar/N_2 atmosphere at a substrate temperature of 573 K. The Cr and Al content was varied by varying the power of the targets. They studied the thermal stability and oxidation resistance of the coating by annealing the samples. Sample was heated between 670 and 1170 K at intervals of 100 K in laboratory air at atmospheric pressure. The heat-up and cool-down phases lasted 10 min, and the holding time was 15 min. After each heating step sample phases were analyzed by XRD analysis. The XRD patterns at 670 and 1170 K are shown in Figure 2-1**.** They concluded that increasing the Al content increased the oxidation temperature of the films [3]. Thermal stability with respect to temperature was studied by J. Lin et al. [32]. They deposited AlCrN coating with two different (0.23 and 0.60) Al atomic percentages by magnetron sputtering process. XRD patterns of both the coatings at different temperatures are shown in Figure 2-2 and Figure 2-3. They showed that fcc-AlCrN phase in $Al_{0.23}Cr_{0.77}N$ and $Al_{0.60}Cr_{0.40}N$ films were thermally stable below 800 and 900 °C, respectively. The degradation of these two Cr-Al-N films started with the formation of h-Cr_2N and Cr_2O_3, accompanied with nitrogen reduction at temperature of 800 and 900 °C, respectively [32].

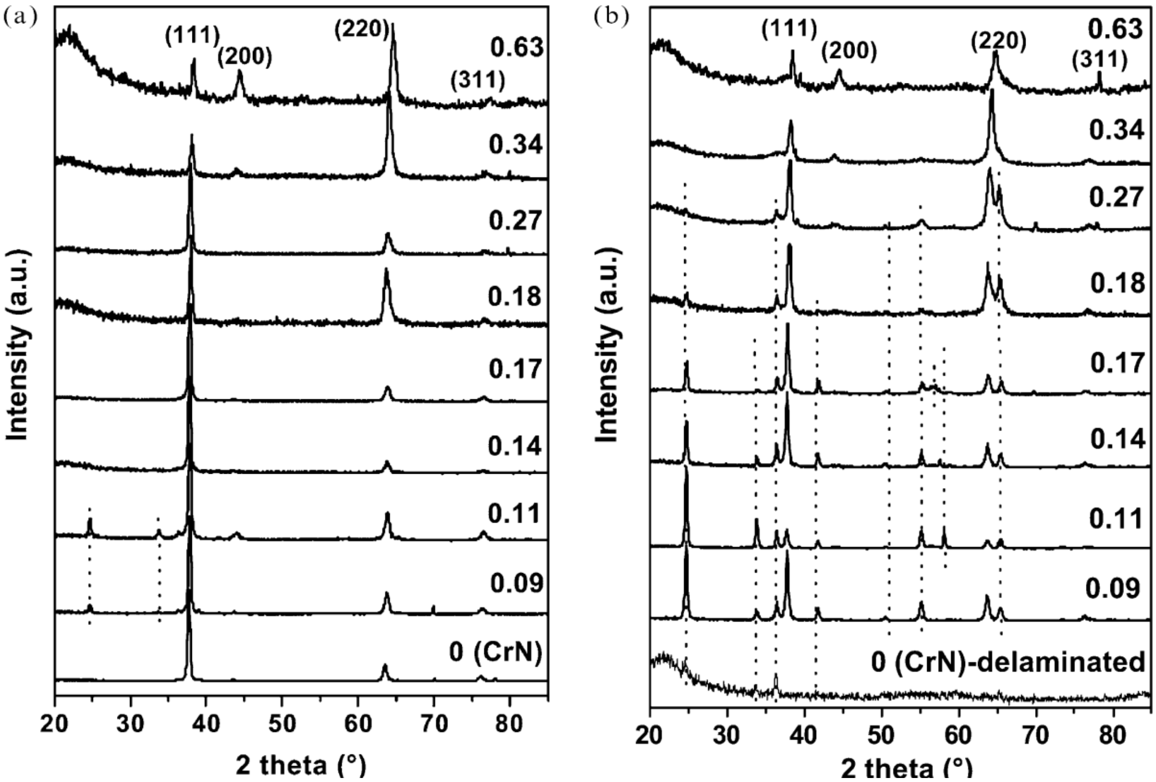

Figure 2-1 XRD spectra of $Al_xCr_{1-x}N$ films after annealing at (a) 770 K and (b) 1170 K.

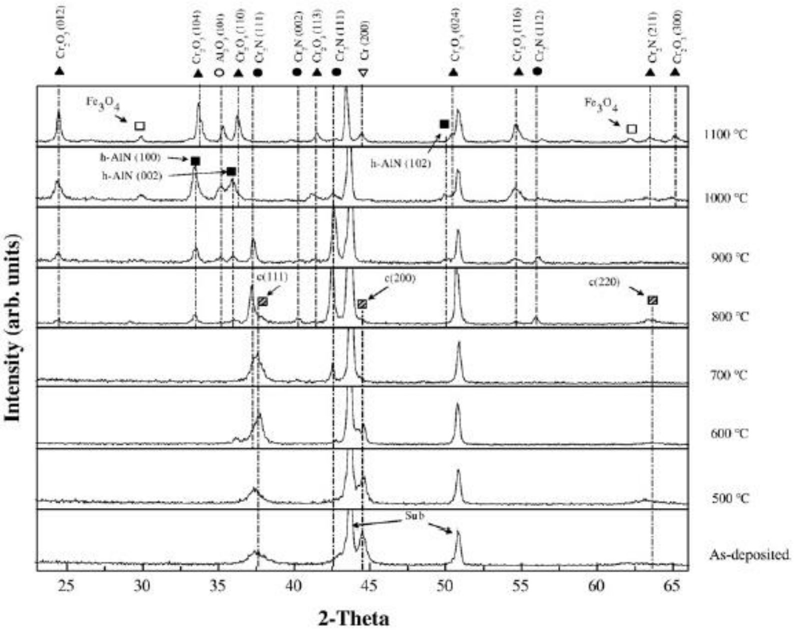

Figure 2-2 XRD patterns of $Al_{0.23}Cr_{0.77}N$ films before and after annealed at different temperatures for 1 h.

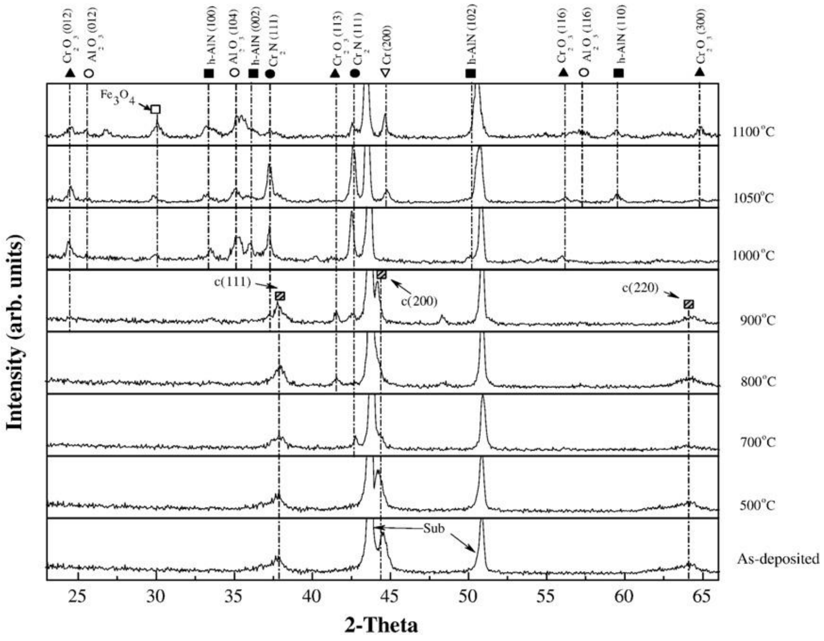

Figure 2-3 XRD patterns of $Al_{0.60}Cr_{0.40}N$ films before and after annealed at different temperatures for 1 h.

2.1.2 Tribological Properties

Hard coatings were deposited to improve the tribological properties. In 2005 Brecher et al. [33] deposited the AlCrN coating on $100Cr_6$ bearings by PVD process. Schematic of equipment and target used for depositing coating is shown in Figure 2-4. The performances of coated bearings were investigated for elastohydrodynamical (EHD) lubrication in spindle bearings. They found that coated bearings have shown tremendous potential on laboratory scale [33]. In same year Xing-Zhao Ding et al. deposited the AlCrN coating by unbalanced magnetron sputtering with Al/Cr ratio from 0 to 0.6 [34]. The coating was deposited on HSS substrate. They plotted the hardness of the coating with respect to Al/Cr ratio and found that hardness increased with increasing Al/Cr ration. Plotted hardness with Al/Cr ratio is shown in Figure 2-5. They also reported that wear resistance of all the AlCrN coatings was six times better than that of the pure chromium nitride coating deposited under similar conditions [34].

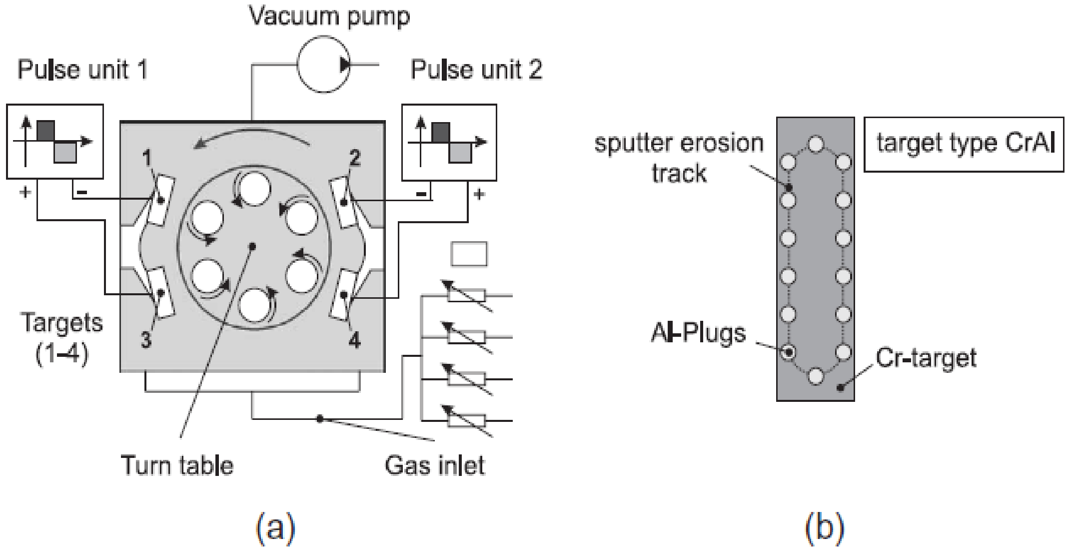

Figure 2-4 PVD experimental setup (a) and target (b) used for depositing AlCrN coating [33].

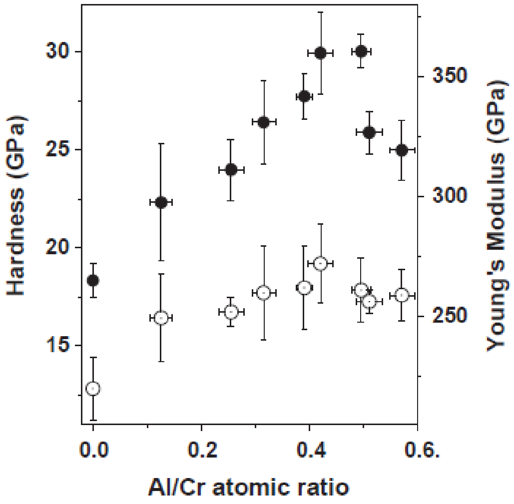

Figure 2-5 Hardness (●) and young modulus (○) value of coating deposited by magnetron sputtering process [34].

Further, a series of $Al_xCr_{1-x}N$ coatings with $0 \leq x \leq 0.7$ were deposited by Ding et al. on high speed steel substrate by vacuum arc reactive deposition process [35]. They observed that all of the as-deposited AlCrN coatings exhibited a higher hardness than CrN, showing a maximum hardness of about 40 GPa at around $x = 0.63$.In 2008, J. L. Mo. et al. [36], analyzed the wear behavior of AlCrN hard against Si_3N_4. Wear rate was investigated by using the CETR multi-functional UMT-2 test system under two sliding conditions (bidirectional and unidirectional). The results showed that AlCrN coating had excellent anti-abrasion properties. Both the normal load in reciprocating sliding test and the sliding velocity in ball-on-disc test had significant influence on the sliding tribological behavior of the AlCrN coating. In the wear mechanism tribo-oxidation played an important role. The oxides were formed during wear test which provided high oxidation resistance and good thermal stability [36].

CHAPTER 3

EXPERIMENTAL PROCEDURE

This chapter presents the experimental methodology for depositing AlCrN coatings and brief description of the various techniques used to characterize the coatings.

3.1 Coating Process – Magnetron Sputtering

Sputtering is a physical vapor deposition (PVD) process used for depositing materials onto a substrate. It is done by ejecting atoms from target materials and condensing the ejected atoms onto a substrate in a high vacuum environment. Coating by PVD method involves purely physical processes such as high temperature vacuum evaporation with subsequent condensation, or plasma sputter bombardment rather than involving a chemical reaction at the surface to be coated as in chemical vapor deposition. Schematic of PVD process flow is shown Figure 3-1.

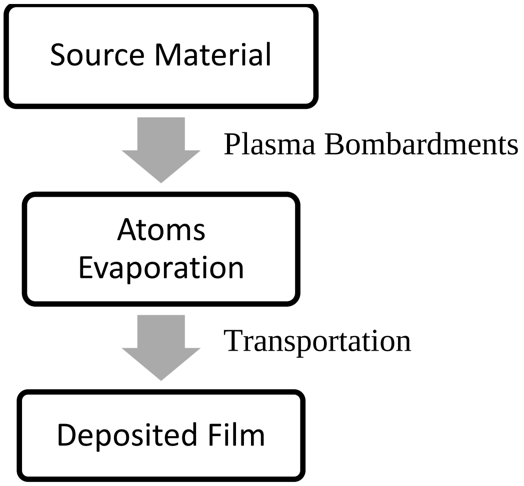

Figure 3-1 Physical Vapor Deposition (PVD) process flow.

The basic idea is simple but the actual mechanisms are quite complex. Electrically neutral Argon atoms are introduced into a vacuum chamber at a pressure of 0.133 to 1.33 Pascals. Argon atoms are ionized by a DC voltage placed between the target and the substrate. Ionized argon atoms create plasma, hot gas-like phase consisting of ions and electrons. Positively charged argon ions are accelerated towards the target. Their collisions with the target eject target atoms, which travel and plate out on the substrate. Electrons released during Argon ionization are accelerated to the anode substrate, subsequently colliding with additional Argon atoms, creating more ions and free electrons in the process, hence repeating the cycle. There are a number of ways to enhance this process. One common way to do this is to use what is known as a magnetron sputtering system. In magnetron sputtering method a strong permanent magnets are placed near the target area. Schematic of placed permanent magnet near the target area is shown in Figure 3-2. Placed permanent magnets create magnetic fields around the target. Induced magnetic field by magnets cause traveling electrons to spiral along magnetic flux lines near the target instead of being attracted toward the substrate. This confined the plasma near the target. Also, electrons travel for a longer distance, increasing the probability of further ionizing Argon atoms. This tends to generate stable plasma with high density of ions. More ions means more ejected atoms from the target, therefore, increasing the efficiency of the sputtering process. Basic components involve in magnetron sputtering process system is shown in Figure 3-3.

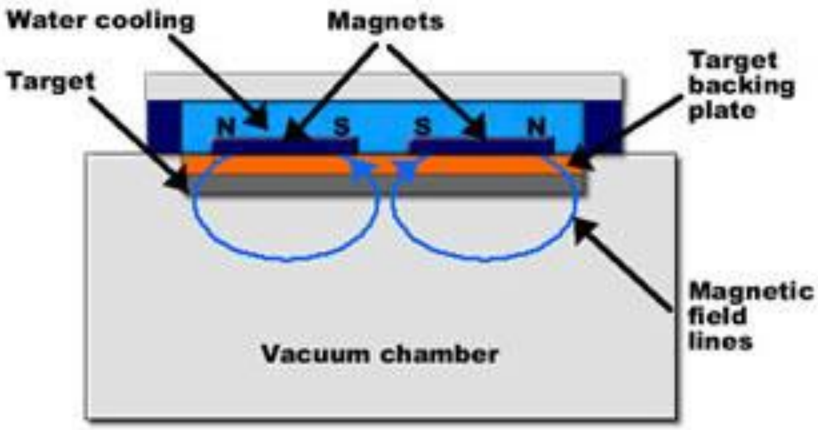

Figure 3-2 Schematic of permanent magnets placed near the target in PVD process[1].

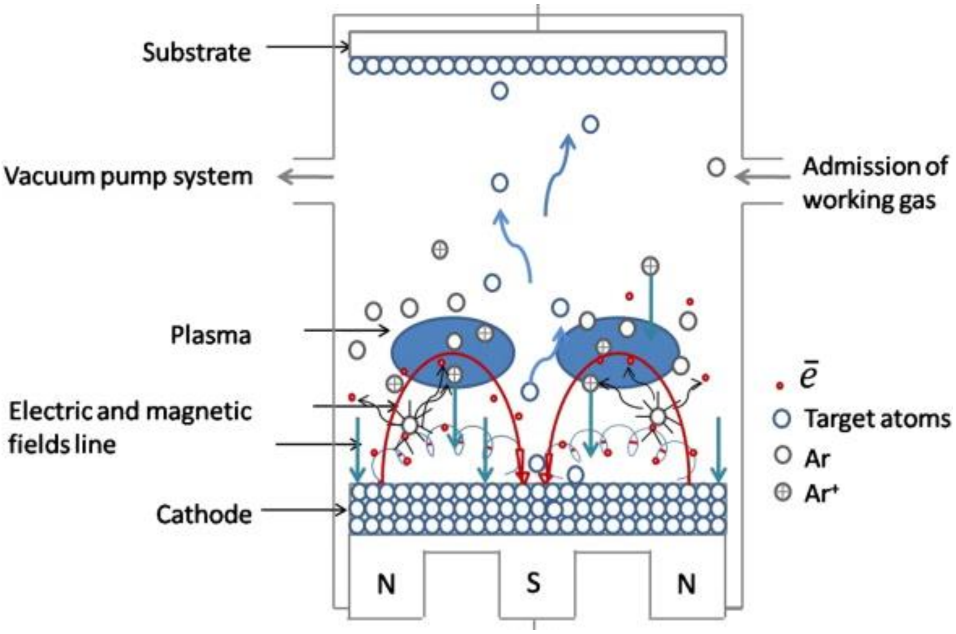

Figure 3-3 The basic components of magnetron sputtering system [37].

---

[1] http://www.dclvacuum.com/tech-3.asp

3.2 Target

In magnetron sputtering process atoms are sputtered from a target so coating composition is mainly affected by target composition. The coating of AlCrN was deposited on H13 tool steel substrate. Aluminium plate with machined and inserted Cr plugs was used as a target. To obtain the different compositions of the coating, two types of target were used:

Target 1 – Aluminium inserted with 8 Cr plugs.

Target 2 – Aluminium inserted with 4 Cr plugs.

Schematic of Target 2, Aluminum inserted with 4 Cr plugs, is shown in Figure 3-4. Coatings were deposited at -30, -50 and -60 V target biasing. The argon flow rate was 15 sccm. Target temperature was around 200^o C.

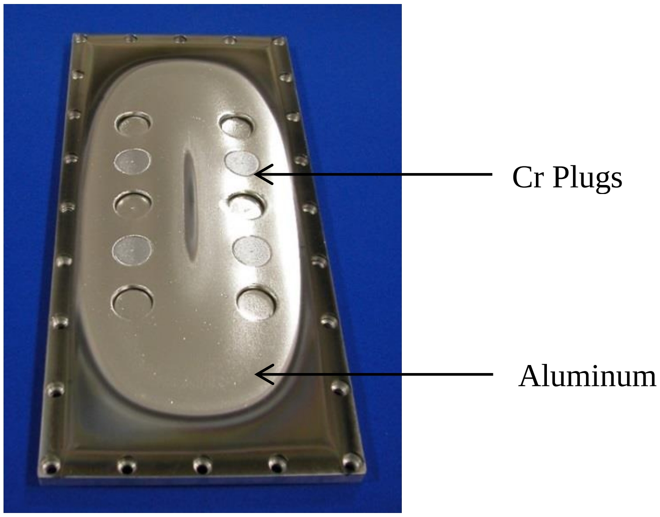

Figure 3-4 Aluminum target inserted with Cr plugs for depositing AlCrN coating.

3.3 EDX and XRD methodology

Energy-dispersive X-ray spectroscopy (EDX) is a technique used for the study of surface chemical compositions. It relies on the principle that unique atomic structure allowing unique set of peaks on its X-ray spectrum. In EDX methodology a high-energy beam of electrons is focused into the sample being studied. The incident beam may excite an electron in an inner shell, ejecting it from the shell while creating an electron hole. Electrons from an outer, higher-energy shell then fills the hole, and the difference in energy between the higher-energy shell and the lower energy shell may be released in the form of an X-ray. The energy of the X-rays emitted from a specimen can be measured by an energy-dispersive spectrometer. The energy of the X-rays is a characteristic of the difference in energy between the two shells of the atomic structure of the element. This allows the elemental composition of the specimen to be measured.

X-ray diffraction is a method to determine the molecular structure of crystal. Crystalline materials diffracts incident beam of X-ray in many different directions. Each crystalline produces a unique X-ray intensity versus diffraction angles. Beams of X-ray are diffracted on the material from defined angles. Diffracted X-ray intensity is recorded with corresponding angle. Crystalline phase was determined by comparing the unknown X-ray intensity by library of known patterns.

3.4 Hardness

The hardness of a coating is obtained by micro-indentation method. In micro-indentation test a diamond indenter of specific geometry is impressed into the surface of the test specimen using a known applied force. The indentation hardness is calculated from the indentation load divided by the projected contact area (equation 1). Vicker indenter was used to obtain hardness value. Vicker indenter is a square pyramid with opposite faces at an angle of 136° and edges at 148° and face angle 68°. To avoid the effect of the substrate indenter penetration should be less than or equal to 10% of the coating. In the presents coating samples, thickness of the coatings were in the range of 3 to 4 µm. Testing was done within 350 nm range. The indentation test was performed at 80 mN load. The size of the indenter impression in this range was too small to measure accurately with the optical technique. The contact area was obtained from loading unloading curve by using equation (2) and equation (3). Schematic of loading unloading curve is shown in Figure 3-5. CSM Micro-Combi tester is used for indentation test is shown in Figure 3-6.

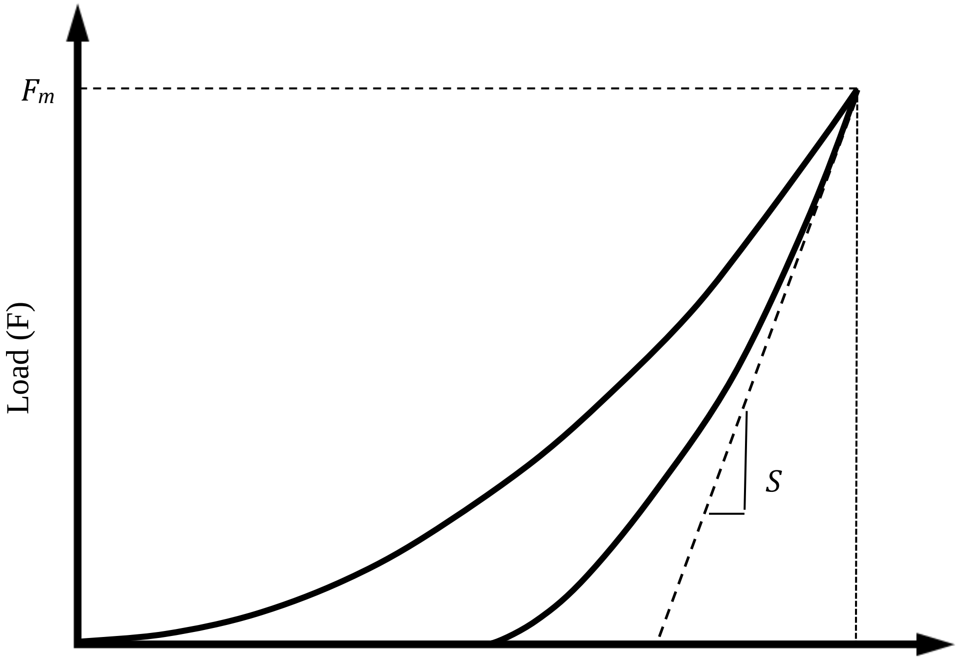

Figure 3-5 Schematic of loading unloading curve for measuring vicker hardness.

$$\boldsymbol{H_v = \frac{F_m}{A_p}} \tag{1}$$

$$\boldsymbol{h_c = h_m - \varepsilon \frac{F_m}{S}} \tag{2}$$

$$\boldsymbol{A_p = C_0 h_c^2 + C_1 h_c + C_2 h_c^{1/2} + \cdots + C_8 h_c^{1/128}} \tag{3}$$

Where,

H_v – Vicker Hardness	F_m – Maximum applied load
A_p – Projected area of the indentation	ε – Poission’s ratio of the material

C_0, C_1, C_2…..C_8 are the geometrical constant for indenter.

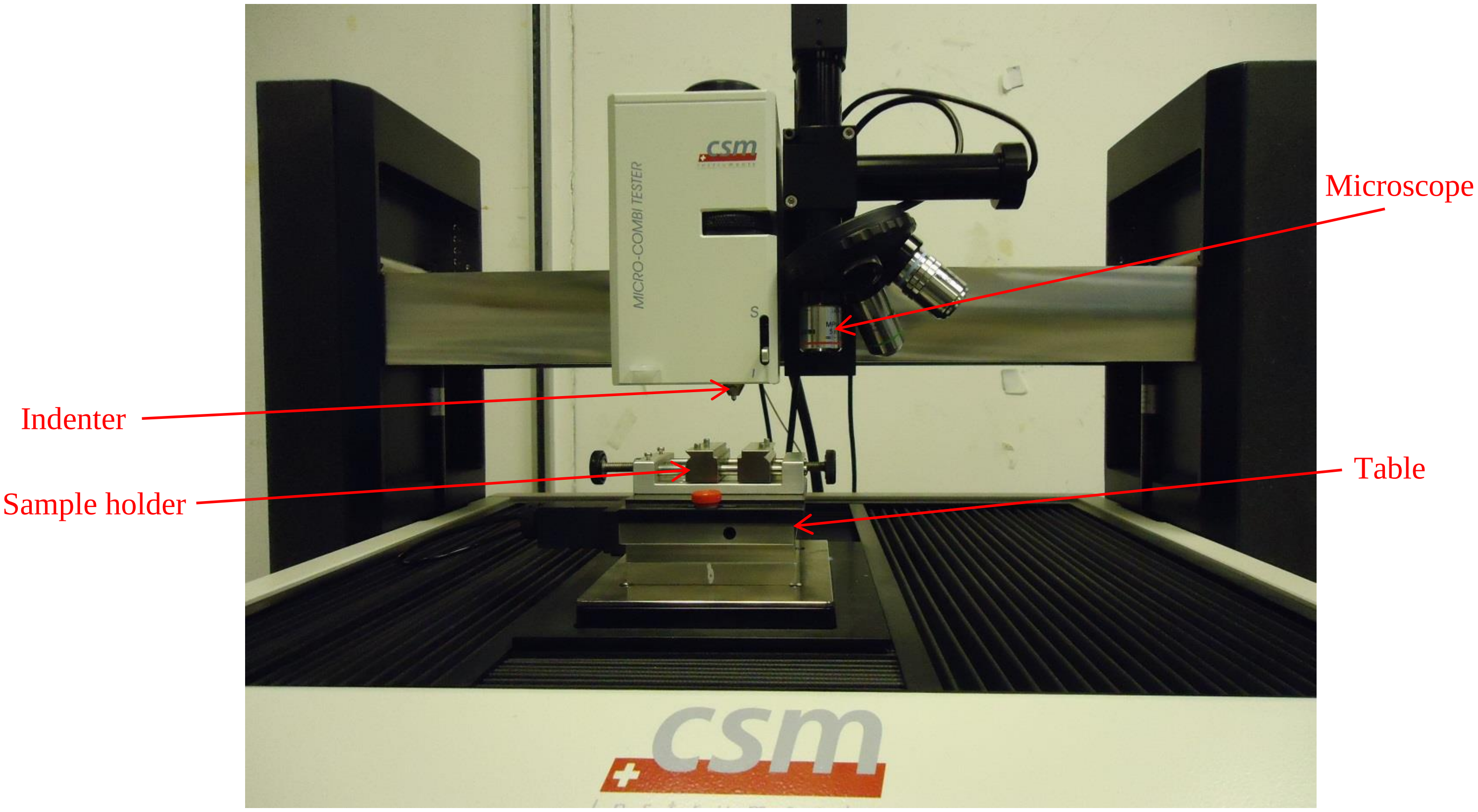

Figure 3-6 Image showing Micro-Combi tester.

3.5 Scratch Test

A scratch tester is used to examine mechanical properties of thin films and coatings, e.g. adhesion, fracture and deformation as per ASTM G 171 03. The technique involves generating a controlled scratch with a sharp tip on a selected area. Schematic of scratch technique is shown in Figure 3-7. The tip material (commonly diamond or hard metal such as (WC)) is drawn across the coated surface under progressive load. At a certain critical load (Lc) the coating will start to fail. According to ASTM C 1624-05 the critical load (Lc) is a function of coating-substrate adhesion, stylus-tip radius, loading rate, mechanical properties of the substrate and the coating, coating thickness, internal stress in coating, flaw size distribution at substrate-coating interface, and friction between stylus-tip and coating.

The scratch test is performed using Micro-combi tester manufactured by CSM Instruments (Figure 3-6). The test is performed by using a sharp diamond Rockwell indenter (I-170), with 100 µm tip radius. The indenter is dragged linearly, 10 mm over a coated surface with a linearly increasing normal load from 0.03 N to 10 N. Loading rate and speed were 4.99 N/mm and 5 mm/min, respectively. The critical loads were very precisely detected by means of an acoustic sensor attached to the load arm but can also be confirmed and collated with observations from a built-in optical microscope. The image of the scratch track is recorded by a microscope. Combination of images to form full scratch track in one image is termed as panorama view. Panorama view of the scratch tracks are generated with their associated acoustic emission signal.

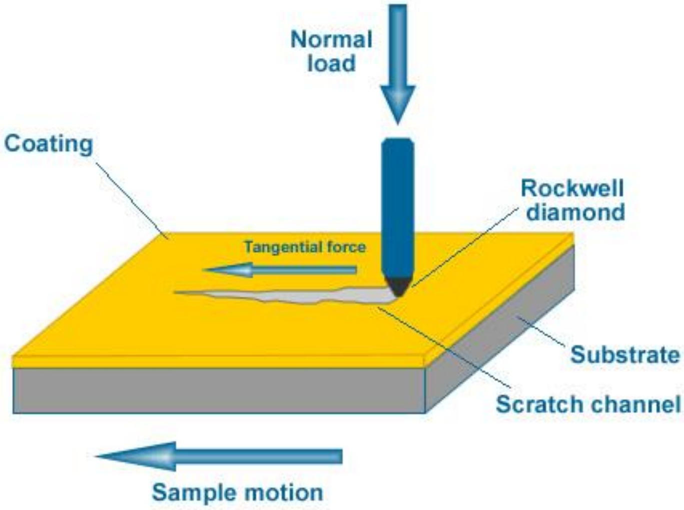

Figure 3-7 Schematic diagram of scratch test*.

*http://www.pvd-coatings.co.uk/pvd-coating-technology/testing-equipment/scratch-tester/

3.6 Creep Test

Creep is very important phenomena in thin film and micro-electromechanical systems application. There are three common procedures for creep measurements [38]:-

- Indentation –load relaxation experiments [39]
- Constant rate of loading rate [40]
- Constant –load indentation experiments (CLI) [41]

Investigation of creep behavior of thin films can be done by using indentation method. Raman and Berriche [41] investigated the creep of polycrystalline Sn and sputtered Al films on Si substrates by this method and found that the indentation creep parameters were analogous to those obtained from conventional creep experiments using bulk materials.

In indentation creep test a constant load is applied with specified loading rate. Load is maintained fixed for certain period of time. During this holding time creep occurs in the material which is measured by recording change in depth with time. Schematic of load profile is shown in Figure 3-8. In the present samples thickness of the coating thickness is in the range of 3 to 4 µm. It has been suggested that to avoid the effect of substrate indenter penetration should be within 10% of the coating thickness [42]. Initially many tests at different loads were carried out from room temperature to 150^o C. Three loads, 20 mN, 40 mN and 60 mN were selected for the test. Indenter penetration depends on the hardness of the coating. Hardness decreases with increasing temperature. Due to the high penetration, testing temperature was restricted to 100^o C. Loading rate was fixed 20 mN/min. At room temperature these loads were not sufficient to penetrate coatings. At room temperature 10 times higher loads of 200 mN, 400 mN and 600 mN were used with 200 mN/min loading rate. Creep analysis was done at four different temperature i.e. room temperature, 50^o C, 75^o C and 100^o C. Temperature of the samples were controlled by Linksys32-Version 2.1.6 made by Linkam Scientific Instruments Ltd. Heating stage incorporated in CSM Micro-combi tester, used for controlling the temperature is shown in Figure 3-9.

.

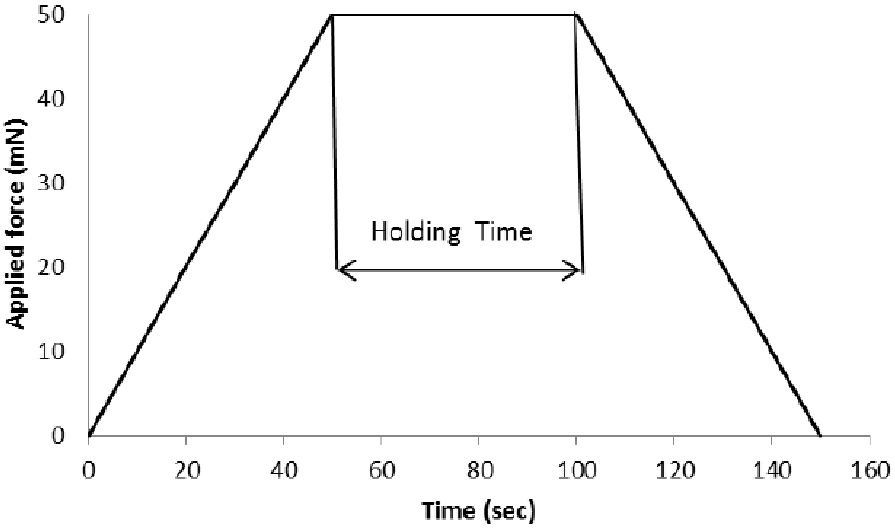

Figure 3-8 Schematic diagram of load profile for creep test.

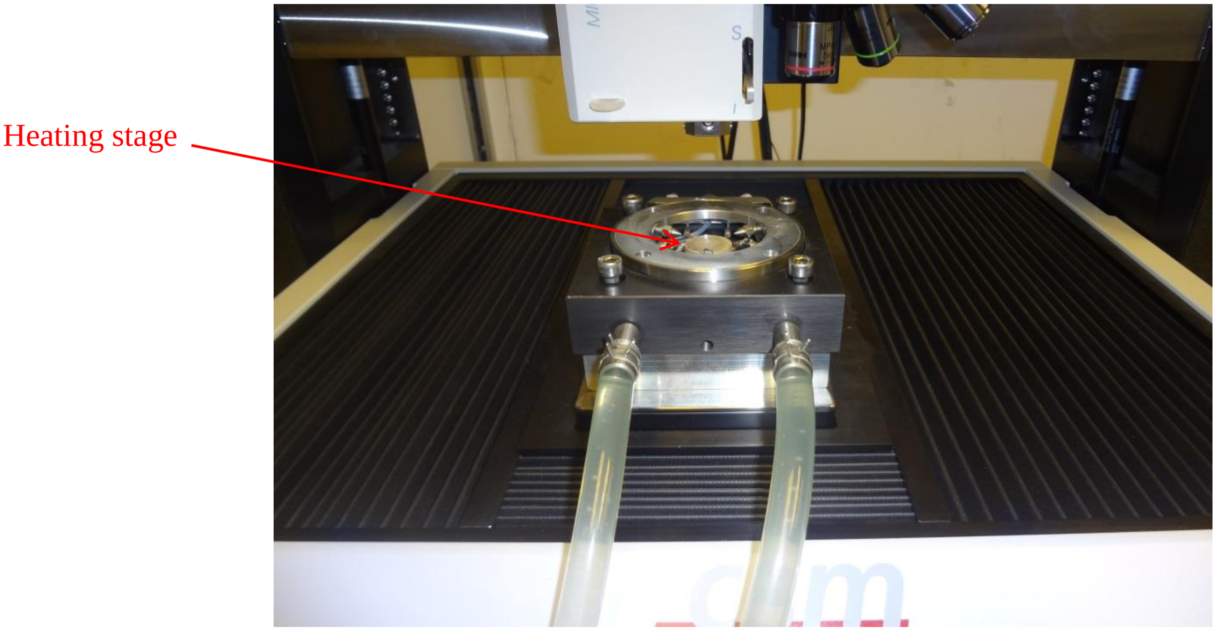

Figure 3-9 Linksys32, heating stage used for high temperature creep testing.

3.7 Wear test

Wear test of coated samples were conducted by using ball-on-disc method. Basic principle of ball-on-disc method is shown in Figure 3-10. In this technique counter material, ball shape, rests on disc shape coated sample under applied normal load. The Disc is rotated with certain speed. Weight of the sample is measured before and after the test. The difference in initial and final weight is divided by normal load and travelled distance gives the wear rate of the coating. Wear rate is calculated in gm/N-m. Wear rate was done against alumina hard balls having 1.5 diameter. Normal load is used as 10 N over a sliding distance of around 100 meters. Wear analysis was done on CSM tribometer shown in Figure 3-11.

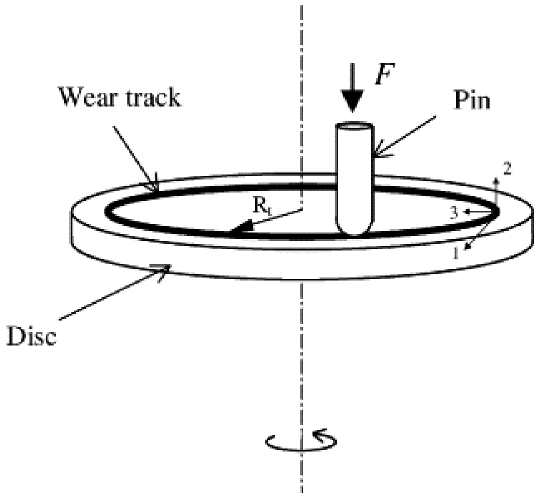

Figure 3-10 Schematic of Ball-on-disc method to study the wear rate [43].

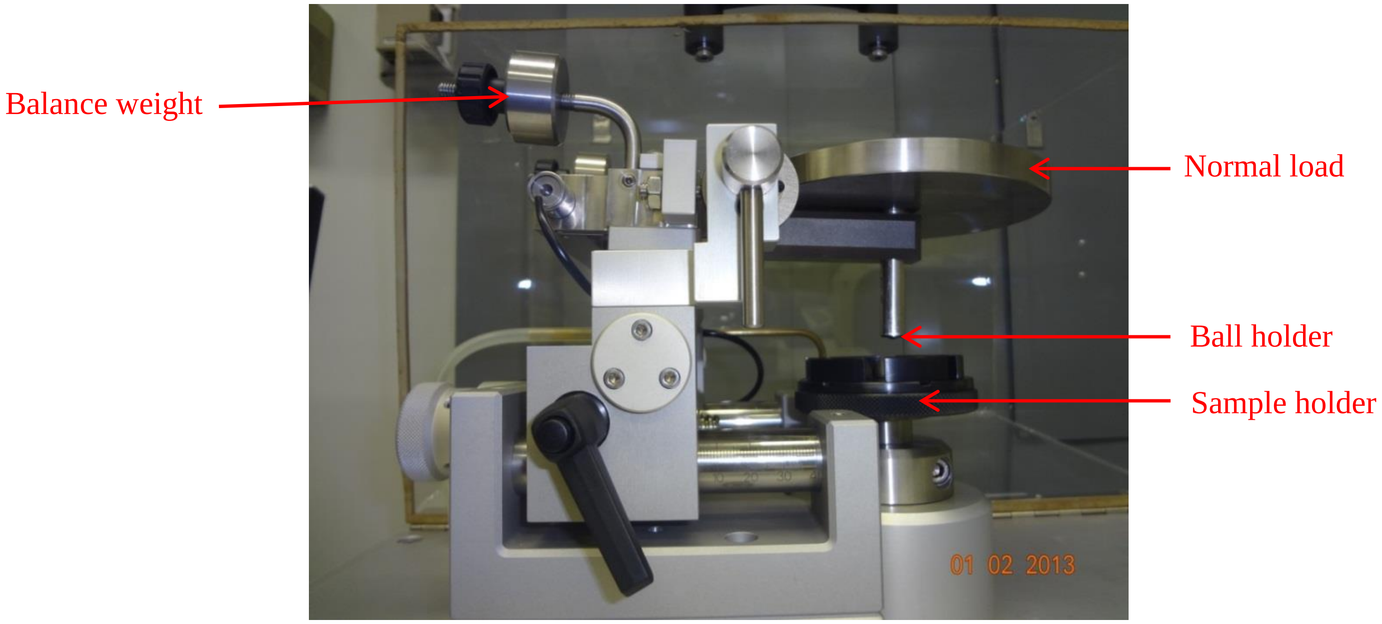

Figure 3-11 Csm tribometer used for wear rate analysis.

CHAPTER 4

RESULTS

This chapter presents the experimental results obtained based on the previous chapter.

4.1 Characterization

The coating was characterized with respect to Cr/Al ratio and target biasing voltages. Characterization was done by measuring compositions, Vickers hardness, surfaces morphologies and cross sectional analysis.

4.1.1 Composition

The compositions of deposited coatings were investigated by using Energy Dispersive X-ray Spectrometry (EDX). The elemental compositions of -30 V and -60 V biased sample deposited by target 1(8 Cr plugs) are shown in Table 4-1. The Cr/Al compositional ratios are 2.12 and 1.97 for biasing voltages of -30 V and -60 V, respectively. This indicates small effect of biasing voltage on the nominal coating composition.

The averages elemental compositions of the coatings deposited using target 1 and target 2 at constant biasing voltage (i.e. -50 V) are shown in Table 4-2. The Cr/Al ratios are around 1.71 and 0.79 for target 1 and 2, respectively. The Cr/Al ratio in the coating is sensitive to the target composition.

Table 4-1 Average elemental weight percentage of coatings deposited using target 1 at -30 V and -60 V biasing.

Bias (V)	Elemental Weight Percentage		
	Cr	Al	N
-30	52.0	24.5	23.5
-60	46.0	23.5	31.0

Table 4-2 Average elemental weight percentage of coatings deposited using target 1 and target 2 at -50V biasing.

Cr plugs	Elemental Weight Percentage		
	Cr	Al	N
4	28.5	36.0	35.0
8	47.0	27.5	24.5

4.1.2 Surface Morphology

Figure 4-1 shows Field Emission SEM micrographs for the surface morphologies of coatings deposited using target 1 at biasing voltages of -30 V and -60 V. In -30 V biased sample small grains are visible while -60 V biased sample shows much finer grains. Similarly Figure 4-2 shows Field emission SEM micrographs for surface morphology of coatings deposited by target 1 and target 2 biased at -50 V. The surface grains are very fine in the coating deposited using target 1. Similar behavior is found in -30 V and -60 V biased sample deposited by using same target. In coating deposited by target 2 large surface grains are clearly visible. The grain sizes are ranging from 100 nm to 300 nm approximately. This might suggest that the surface average grain size decreases with increasing Cr content in the coating.

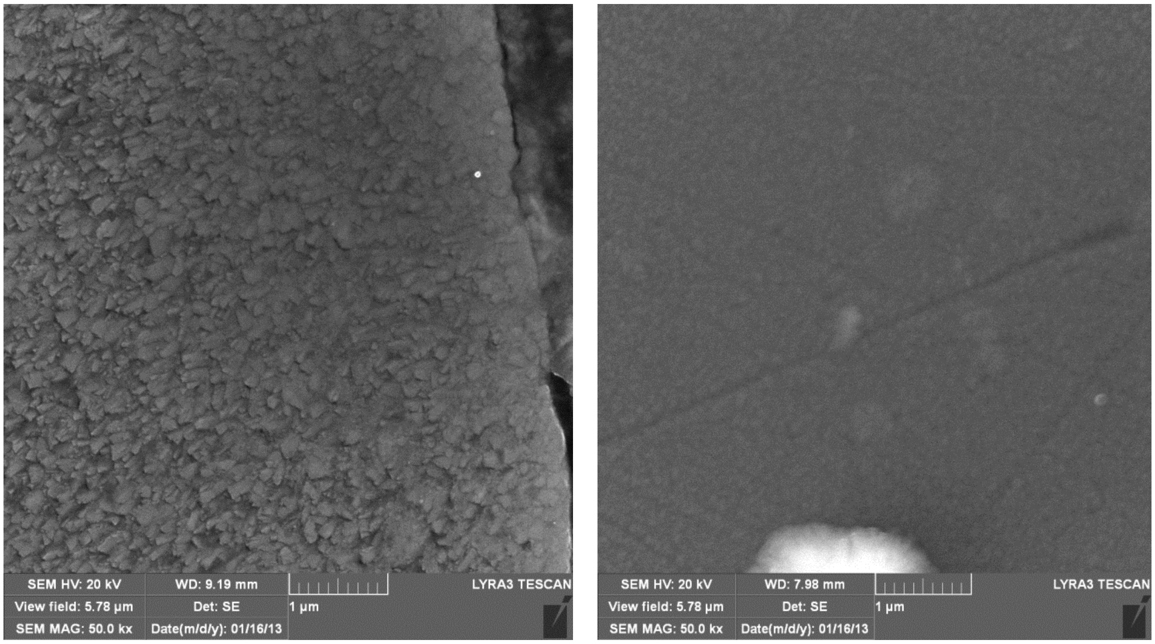

(a) (b)

Figure 4-1 Field Emission SEM micrographs of coating surfaces deposited using target 1 at (a) -30 V and (b) -60 V biasing.

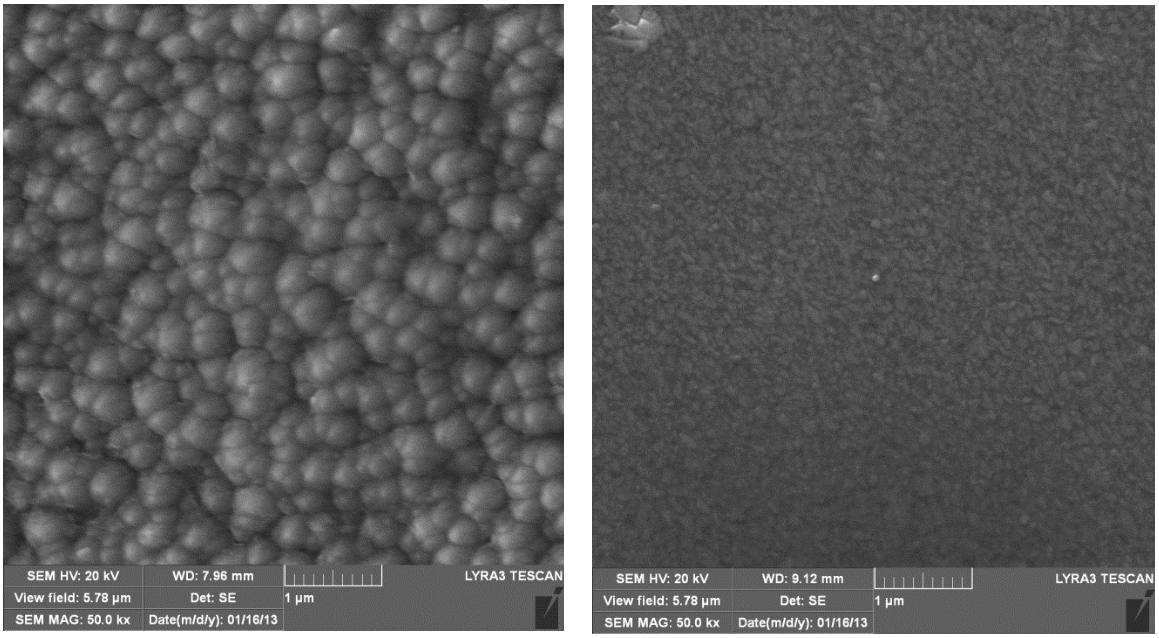

(a) (b)

Figure 4-2 Field Emission SEM micrographs of coating surfaces deposited by using (a) Target 2 (b) Target 1 at -50 V Biasing.

4.1.3 Cross sectional Analyses

Field Emission SEM micrographs of the coating cross sections are shown in Figure 4-3 to Figure 4-6. The image show that each coating seems to consist of two layers. Bulk coating layer and an interface layer between the coating and the substrate. The bulk coating layer is the major part of the coating. Interface layer was in the range of 500 nm in thickness. EDX analysis was done at different locations across the coating thickness. Compositions are shown in three positions, A- near the interface layer, B- approximately mid thickness of the bulk and C- near the surface of the coating. Elemental compositions along the coating thickness in -30 V biased coating are shown in Table 4-3. Chromium content decreased from interface layer to the bulk of the coating while nitrogen content increased. Variation in the Al content was much less than that for Cr. Similarly, elemental compositions along the coating thickness for all other coatings are shown in Table 4-4 to Table 4-6. In all coatings, nitrogen content increased from interface layer to the bulk coating while chromium content decreasing. Small amount of argon (Ar) was found in the interface layer.

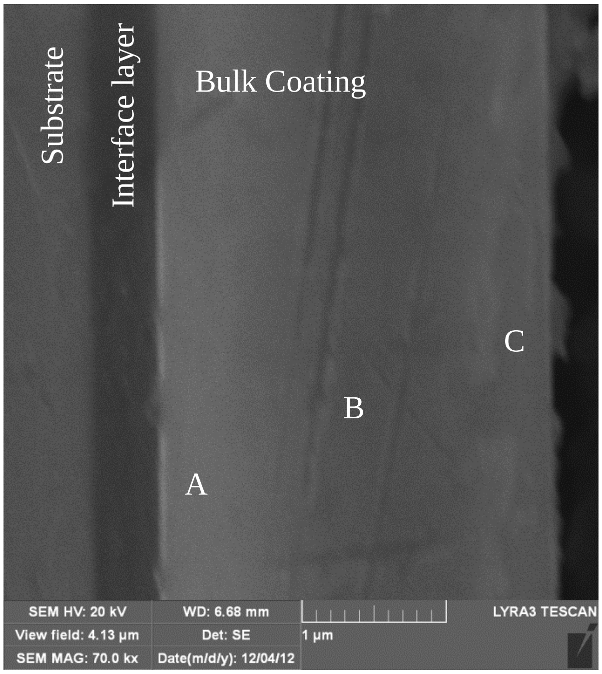

Figure 4-3 Field Emission SEM micrographs showing an interface layer between substrate and bulk of coating deposited using target 1 at -30 V biasing.

Table 4-3 Elemental compositions across the coating thickness of coating deposited using target 1 at -30 V biasing.

Elements	Interface Layer	Position in Bulk Coating		
		A	B	C
Cr	69.3	58.2	44.7	30.0
Al	25.4	24.4	25.1	21.7
N	4.5	17.1	30.1	48.3
Ar	0.8	0.3	0.1	-

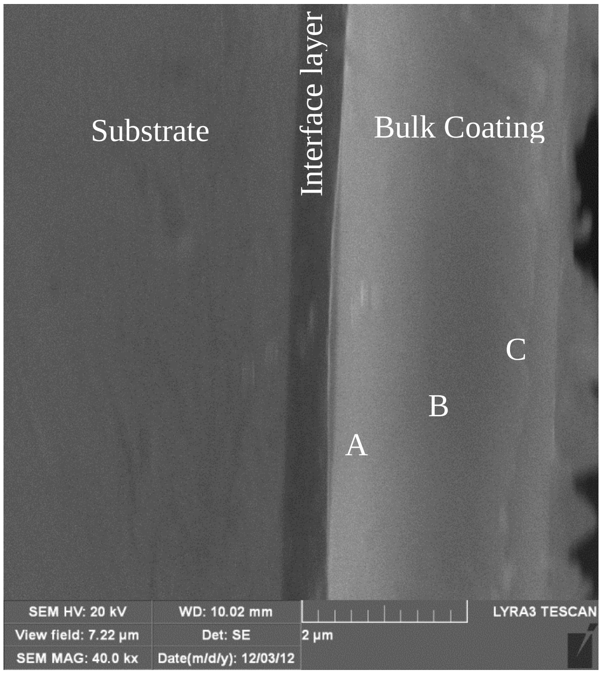

Figure 4-4 Field Emission SEM micrographs showing an interface layer between substrate and bulk of coating deposited using target 1 at -60 V biasing.

Table 4-4 Elemental compositions across the coating thickness of coating deposited using target 2 at -60 V biasing.

Elements	Interface Layer	Position in Bulk Coating		
		A	B	C
Cr	84.2	66.0	42.1	27.6
Al	14.4	23.6	26.1	22.4
N	0.3	10.2	31.7	49.9
Ar	1.1	0.3	-	0.1

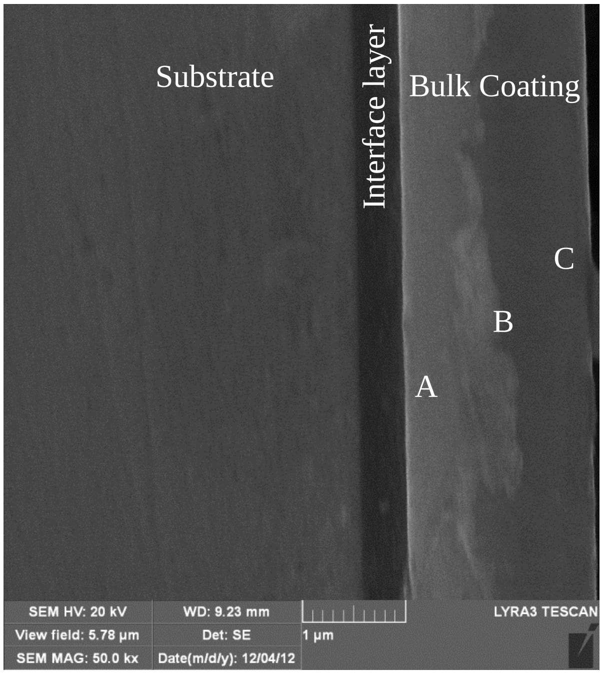

Figure 4-5 Field Emission SEM micrographs showing an interface layer between substrate and bulk of coating deposited using target 2 at -50 V biasing.

Table 4-5 Elemental compositions across the coating thickness of coating deposited using target 2 at -50 V biasing.

Elements	Interface Layer	Position in Bulk Coating		
		A	B	C
Cr	38.2	28.0	22.1	17.7
Al	47.0	38.2	34.0	30.0
N	14.2	33.8	43.9	52.1
Ar	0.6	-	-	0.2

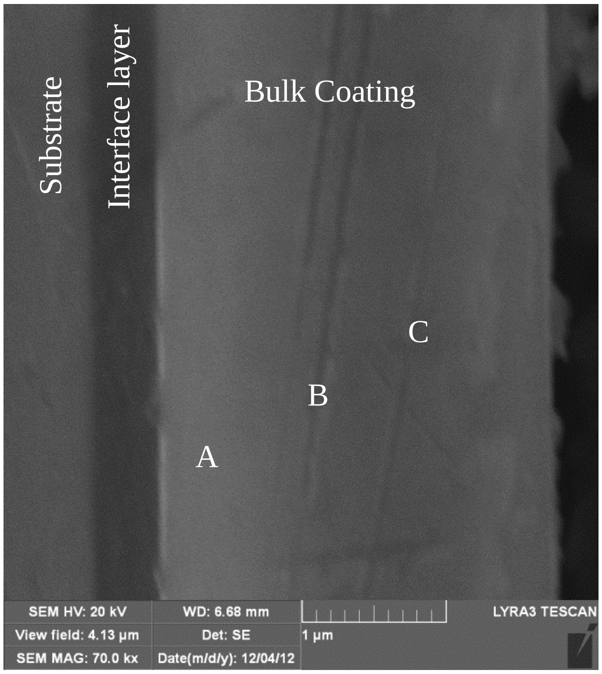

Figure 4-6 Field Emission SEM micrographs showing an interface layer between substrate and bulk of coating deposited using target 1 at -50 V biasing.

Table 4-6 Elemental compositions across the coating thickness of coating deposited using target 1 at -50 V biasing.

Elements	Interface Layer	Position in Bulk Coating,-50		
		A	B	C
Cr	56.9	49.1	41.4	36.6
Al	37.2	30.1	26.0	26.2
N	4.8	20.8	32.6	37.0
Ar	1.1	-	-	0.3

4.1.4 Phases

XRD patterns of the coatings deposited by target 1 and target 2 at different biasing voltages along with the substrate (H13 tool steel) are shown in Figure 4-7. In the coatings deposited using target 1 showed the peaks of Cr(Al)N belonging to the (111) obtained at around 38^o [44, 45]. Coating deposited by target 1 showed same peaks at each biasing voltages. All peaks were localized between chromium nitride and aluminium nitride suggesting a possible complete solution of chromium and aluminium nitirdes. The coating deposited by using target 2 showed a peak of phase Cr_2N at around $2\theta = 50^o$ [9] along with the peak Cr(Al)N at around 38^o. Several peaks of substrate are obtained at different angles.

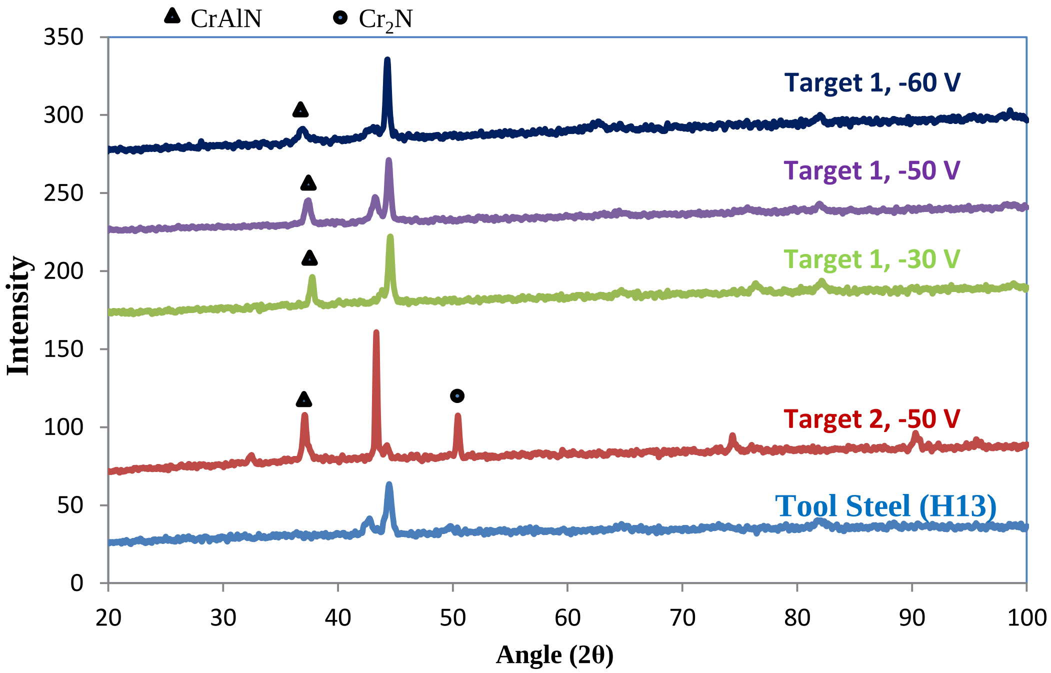

Figure 4-7 XRD pattern of substrate (H13 too steel) and AlCrN coating deposited by using target 1 and target 2 at different biasing voltages.

4.1.5 Hardness

The objective of depositing the AlCrN coating was to enhance the surface properties of substrate. Hardness is one of the key parameter to control the tribological properties. The hardness of all samples were obtained by using micro indentation technique. Table 4-7 shows the Vickers hardness value of the coatings. According to the tabulated values, coating deposited at -50 V target biasing, the hardness increased with Cr content in the target. Also the hardness was appeared to increasing with increasing the biasing voltage. These coatings are much harder than the substrate (H13 tool steel). Highest vicker hardness was found for -60 V biased coating deposited using target 1.

Table 4-7 Average Vickers hardness of the coatings along with the standard deviation of 5 consecutive tests.

Target	Biasing Voltage	Vicker Hardness (H_V)	Std. Dev.
Target 1 (8 Cr plugs)	-30	3835	367
	-50	4935	626
	-60	5185	740
Target 2 (4 Cr plugs)	-50	1925	167
H13 Tool steel	-	251	21

4.2 Scratch Test

4.2.1 Target 1 Coating – Effect of Biasing Voltage

A panorama view of the scratch track for the coating produced by using target 1 at -30 V biasing is shown in Figure 4-8. The accompanying acoustic emission (AE) generated during scratching is also displayed. The critical load (Lc) at which coating starts to fail corresponds to a sudden increase in the AE amplitude. The critical load is a complex parameter and depends on substrate adhesion, stylus-tip radius, loading rate, mechanical properties of substrate and coating, coating thickness, internal stresses in coating, flaw size distribution at substrate-coating interface and friction between stylus-tip and coating [46]. In the present analysis all the parameters were kept common. Figure 4-8 indicates that the critical load corresponds to approximately 3.8 N. Once failure started it continued to the end of the track with high fluctuation in the AE amplitudes. Figure 4-9 exhibits the scratch track for the coating deposited using target 1 at -60 V biasing. The critical load (L_c) is again around 3.8 N. The generated AE signals shows much higher peaks in -60 V biased sample as compared to -30 V biased sample.

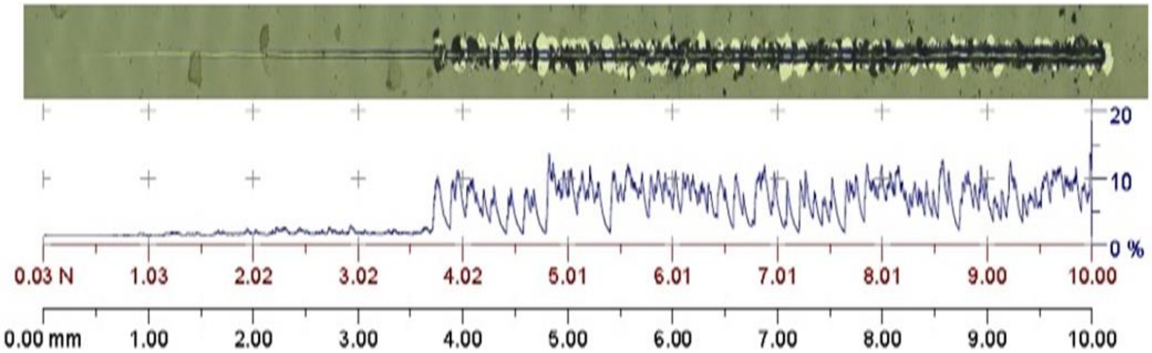

Figure 4-8 Scratch test with linearly increasing load 0.03 – 10 N on coating deposited using target 1 at -30 V biasing.

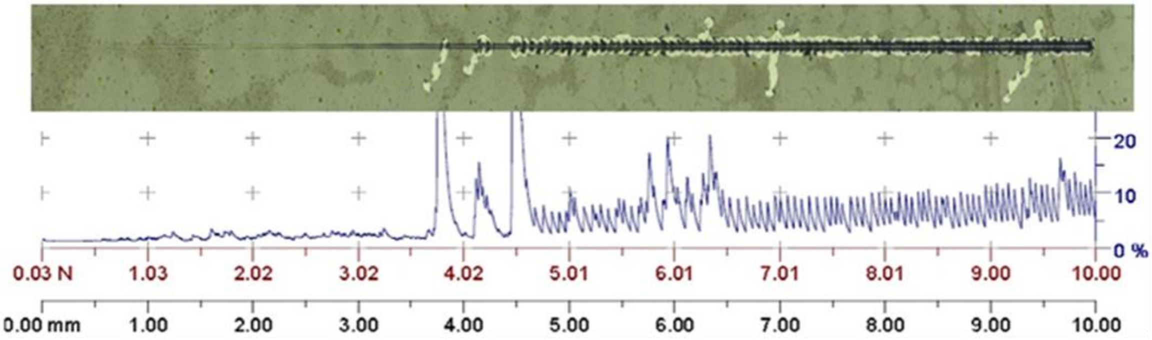

Figure 4-9 Scratch test with linearly increasing load 0.03 – 10 N on coating deposited using target 1 at -60 V biasing.

The SEM micrographs at the end point of the scratch track were taken. Multi- layered coating delamination in -30 V and -60 V biased sample are shown in Figure 4-10 and Figure 4-11, respectively. It appears in both coating samples that coatings are multi-layered. The coating was chipped off from different layers. Trackside delamination was much higher in -60 V biased sample. In -30 V biased sample coating was delaminated near the scratch track. In -60 V biased sample coating delaminated far from the scratch track which created branch like cracks. Trackside delamination of -30 V and -60 V biased sample are shown in Figure 4-12 and Figure 4-13, respectively.

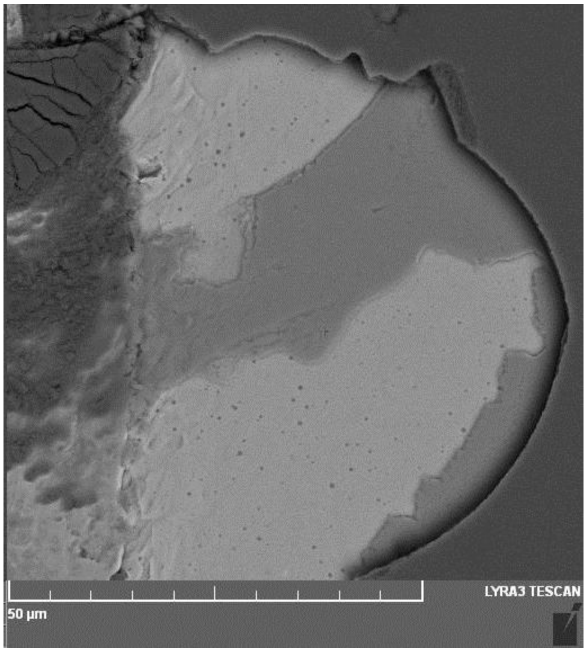

Figure 4-10 SEM image showing multi-layered structure coatings deposited using target 1 at -30 V biasing.

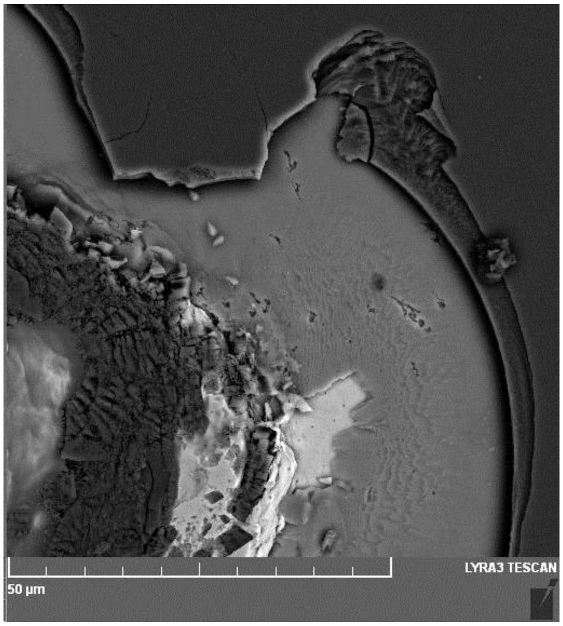

Figure 4-11 Field emission SEM micrograph showing multi-layered structure of coating deposited using target 1 at -60 V biasing.

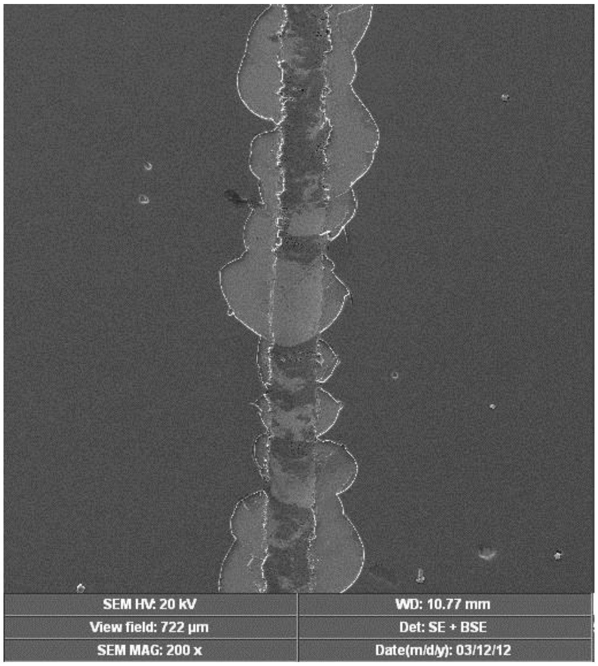

Figure 4-12 Field Emission SEM micrograph showing track side delamination of coating deposited using target 1 at -30 V biasing.

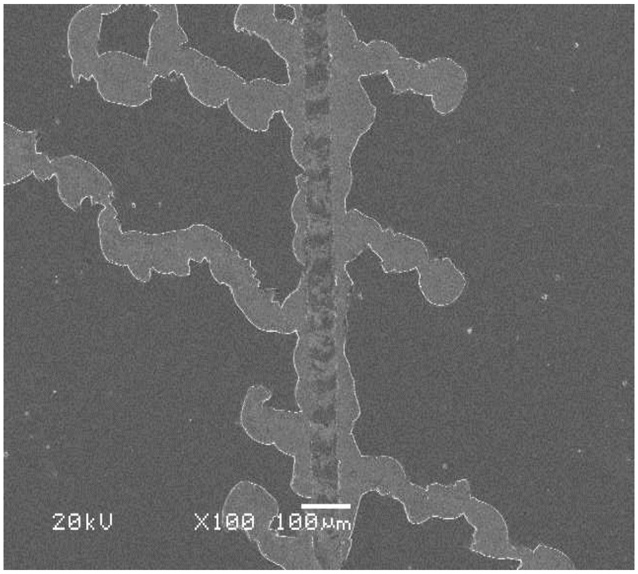

Figure 4-13 Field Emission SEM micrograph showing branching like trackside delamination of coating deposited using target 1 at -60 V biasing.

Elemental mapping was done at the scratch end point. Field emission SEM micrographs show that coating was chipped off from the substrate for both biasing voltages coating samples. Elemental mapping of -30 V biased coating sample is shown in Figure 4-14. Mapping analysis shows that the substrate was exposed in -30 V biased sample. Part of the coatings was present on the indenter path. Elemental mapping analysis for -60 V biased sample is shown in Figure 4-15. In -60 V biased sample coating was chipped off but substrate was not exposed. Coating elements are found along the scratch track. Elemental mapping analysis for -60 V biased sample showed that coating element was observed rather than substrate. This indicates that adhesion is better in -60 V than -30 V biased samples.

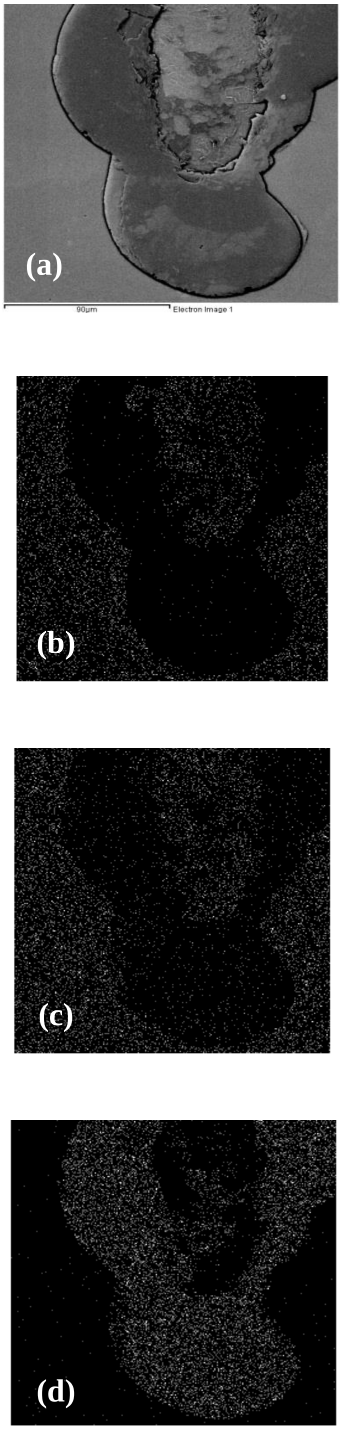

Figure 4-14 Image showing elements (b) Al (c) Cr and (d) Fe at the (a) scratch end point of coating deposited using target 1 -30 V biasing.

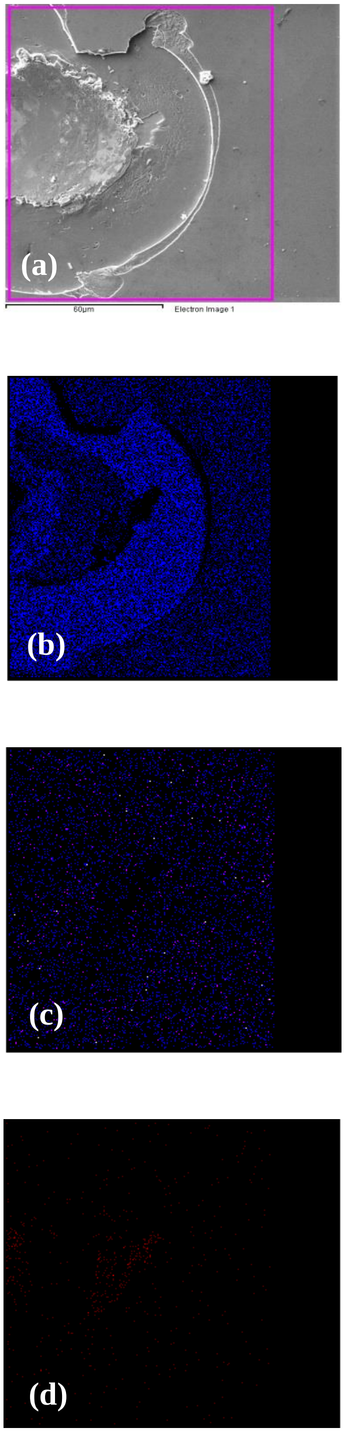

Figure 4-15 Image showing element (b) Al (c) Cr and (d) Fe at the (a) scratch end point of coating deposited using target 1 at -60 V biasing.

4.2.2 Effect of Cr/Al content

Similar scratch analysis was done to analyze the effect of Cr/Al content on the scratch resistance of the coating. Panorama view of scratch track of coating deposited using target 2 and target 1 at constant voltage of -50 V are shown in Figure 4-16 and Figure 4-17, respectively. The critical loads are around 2.5 N and 3.9 N for target 2 and target 1 coating, respectively. This is consistent with the previous results which showed that critical load for target 1 coating at -30 V and -60 V biased samples were around 3.8 N. Acoustic emission signal in panorama view of target 1 coating sample (biased at -50 V) is similar to the coatings biased at -30 V and -60 V biased sample (both are deposited using target 1). AE signal was almost constant during the deformation. Whereas coating deposited using target 2 coating showed increase in acoustic emission signal up to a constant value. After attaining a constant value it remained approximately constant along the scratch track. Acoustic emission signal became constant at around 7 N.

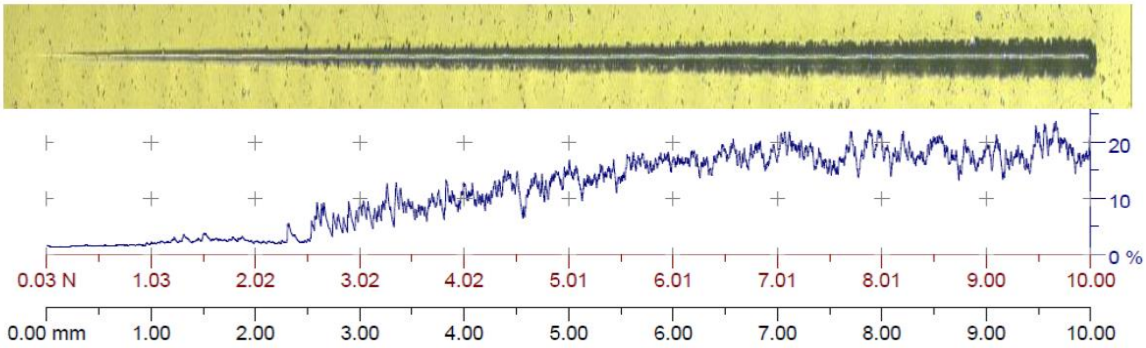

Figure 4-16 Scratch test with linearly increasing load 0.03 – 10 N on coating deposited using target 2 at -50 V biasing.

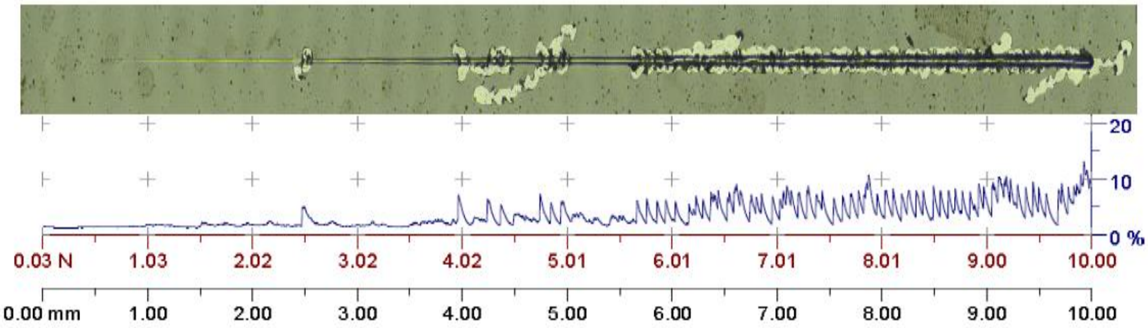

Figure 4-17 Scratch test with linearly increasing load 0.03 – 10 N on coating deposited using target 1 at -50 V biasing.

SEM images were taken of the scratch track. Images at the fractured point showed that coatings apparently were multi-layered. It appears that the coating was chipped off as layers. Figure 4-18 and Figure 4-19 show multi-layered coatings samples deposited by target 1 and target 2, respectively. Target 1 coating sample exhibited large trackside delamination. Large trackside delamination is also visible in the panorama view. The coating deposited by target 2 was not chipping off from the substrate. There was no visible trackside delamination.

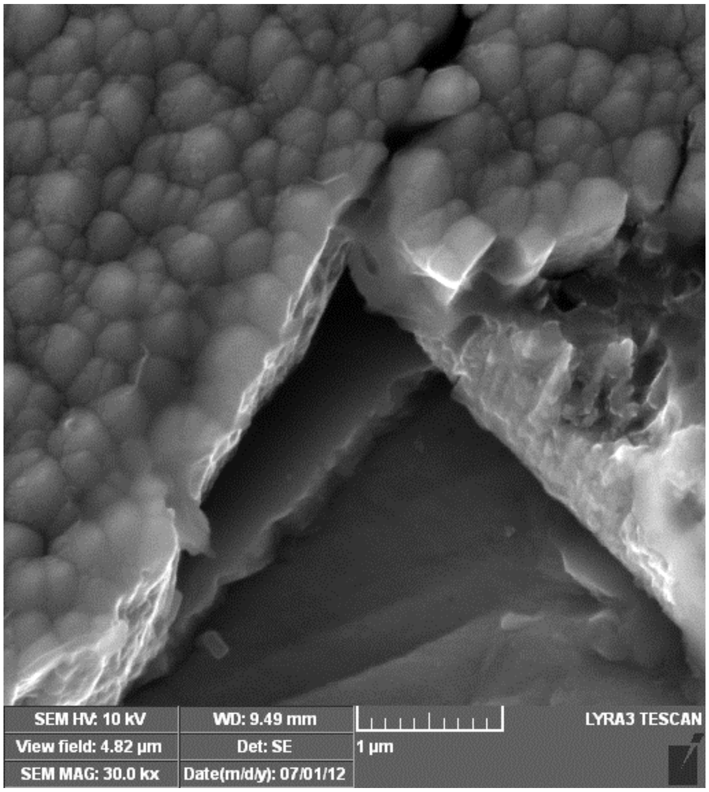

Figure 4-18 Field Emission SEM micrograph showing multi-layered coating deposited using target 2 at -50 V biasing.

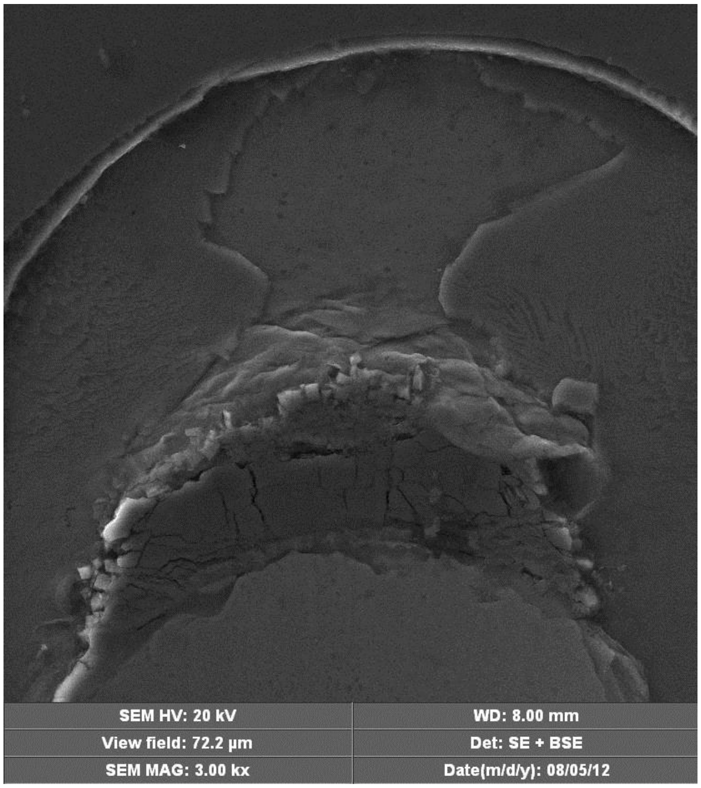

Figure 4-19 Field Emission SEM micrograph showing multi-layered coating deposited using target 1 at -50 V biasing.

As it was visible in scratch track that there was a large coating delamination in target 1 coating sample but no coating delamination was observed in target 2 coating sample. To analyze the coating adhesion of different layers elemental mapping analysis was done for Cr, Al and Fe content. It showed that substrate was exposed in target 1 coating sample but part of coating was delaminated. Some coating chips were embedded in the track. In target 2 coating sample no coating delamination was observed. Mapping analysis for Cr, Al and Fe content for target 2 and target 1 coating sample are shown in Figure 4-20 and Figure 4-21, respectively.

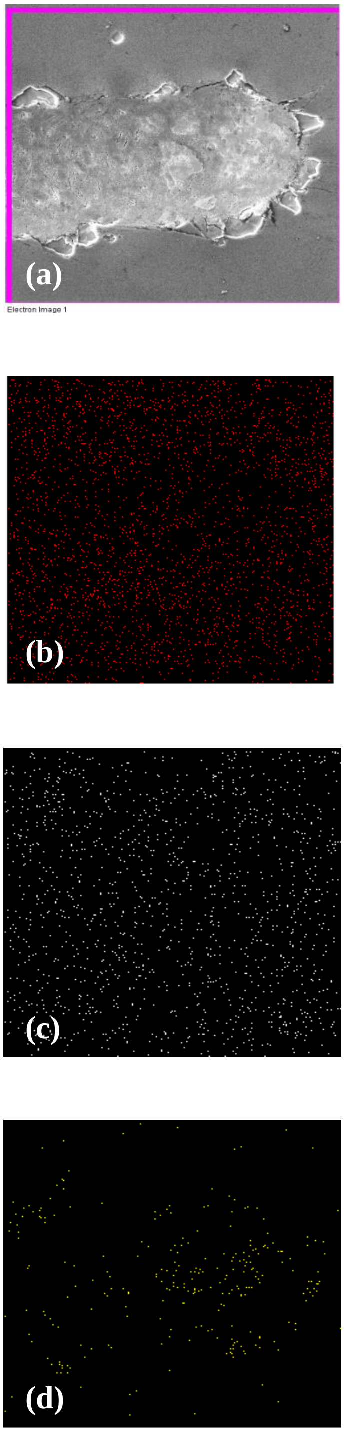

Figure 4-20 Image showing element (b) Al (c) Cr and (d) Fe at the (a) scratch end point of the coating deposited using target 2 at -50 V biasing.

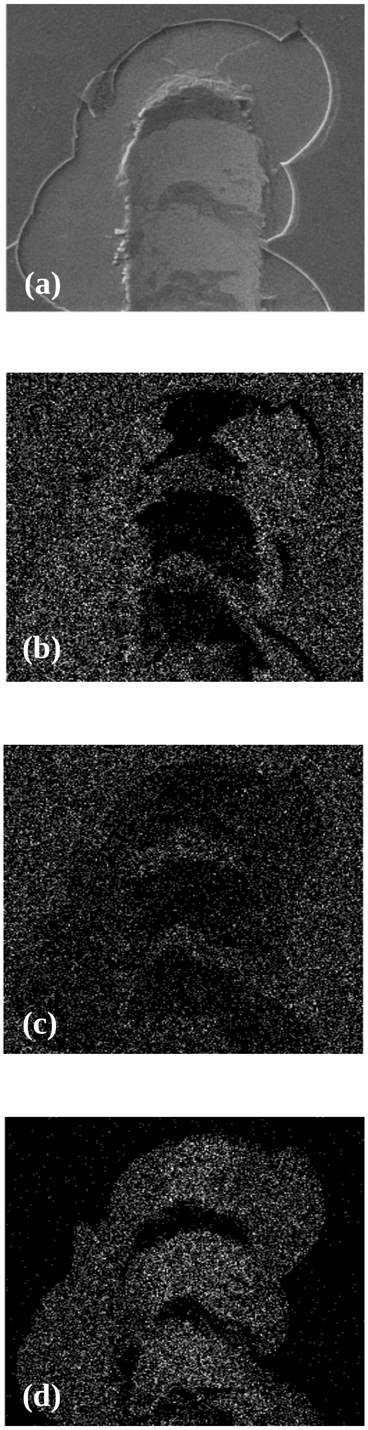

Figure 4-21 Image showing element (b) Al (c) Cr and (d) Fe at the (a) scratch end point of the coating deposited by using 8 Cr plugs biased at -50 V.

4.3 Creep

Creep test was performed on coating deposited by using target 1 (8 Cr plugs) and target 2 (4 Cr plugs). Creep curves at room temperature for 200 mN, 400 mN and 600 mN loads are shown in Figure 4-22 to Figure 4-24. At room temperature, during holding time, plastic deformation occurred in target 2 coating sample only. There was no plastic deformation in target 1coating. This behavior was observed consistently at all loads. Change in depth for target 2 coating sample was not constant. It decreased with holding time. Higher creep resistance in target 1 coating sample indicates that creep resistance increased with increasing Cr/Al ration in the coating. Indenter penetration before starting the creep was deeper in target 2 coating because of lower hardness value.

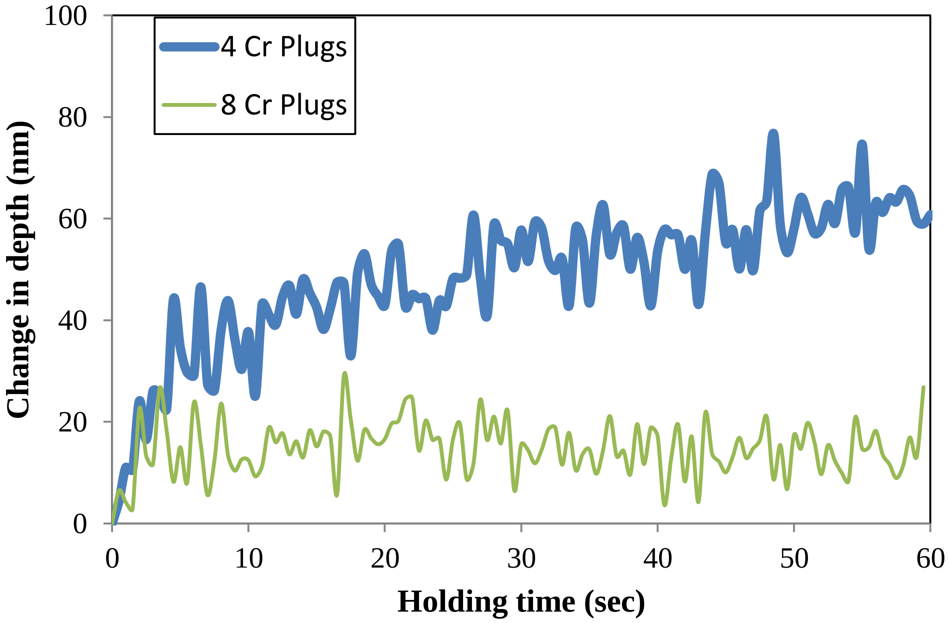

Figure 4-22 Variation in the penetration depth with load-holding time at room temperature by 200 mN load.

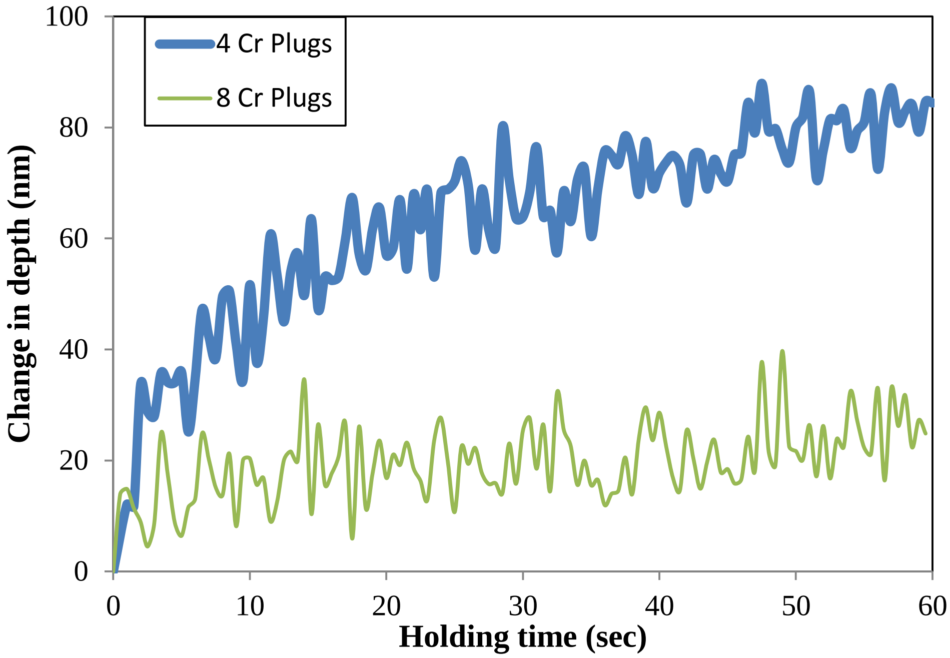

Figure 4-23 Variation in the penetration depth with load-holding time at room temperature by 400 mN load.

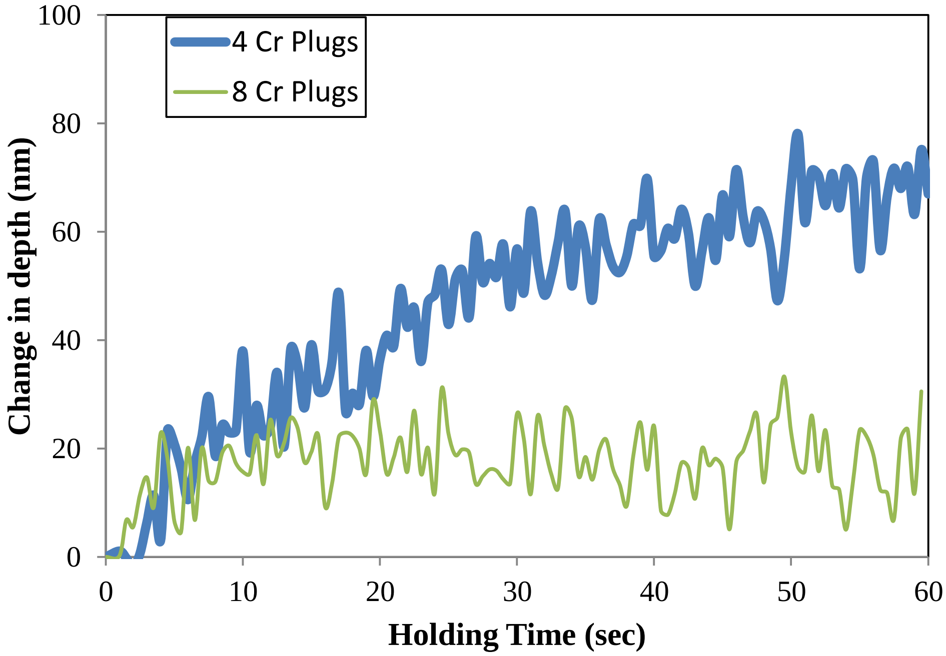

Figure 4-24 Variation in the penetration depth with load-holding time at room temperature by 600 mN load.

Creep tests were performed at 50^o C, 75^o C and 100^o C. Creep curves at 50^o C are shown in Figure 4-25 to Figure 4-27. At this temperature creep effect was found in both the coating. Creep curves were linear with time. The creep rate was lower for higher Cr/Al content coating (deposited by target 1). The same behavior was found at room temperature. This showed that creep resistance was higher for higher Cr/Al ratio. Total change in depth for target 1 coating was approximately 185 nm, 160 nm and 150 nm for 20 mN, 40 mN and 60 mN loads, respectively. Similarly, changes in depth for target 2 coating was approximately 271 nm, 276 nm and 510 nm for 20 mN, 40 mN and 60 mN applied load, respectively. Creep curves at 75^o C are depicted Figure 4-28 to Figure 4-30 for 20 mN, 40 mN and 60 mN, respectively. Creep curves at 100^o C are shown in Figure 4-31 to Figure 4-33 for 20 mN, 40 mN and 60 mN load, respectively. At all temperatures, creep behavior was similar. Creep resistance was found higher for higher Cr/Al content sample. At 100^o C total change in depth increased with increasing load. In general hardness is a temperature dependent property. It decreases with increasing temperature. Indenter penetration increased with increasing temperature. At 75^o C creep test, coating deposited by using target 2, indenter starting depth was around 15%, 28% and 39% for 20 mN, 40 mN and 60 mN, respectively. At 100^o C creep, target 2 coating, indenter starting point was around 20%, 38% and 57% for 20 mN, 40 mN and 60 mN, respectively. Indenter penetration during holding time also increased more. Increasing temperature and load may have increased the substrate interference in the creep behavior. Creep rate was calculated by the slope penetration depth line with holding time. Calculated creep rate for target 1 and target 2 coatings are shown in Table 4-8.

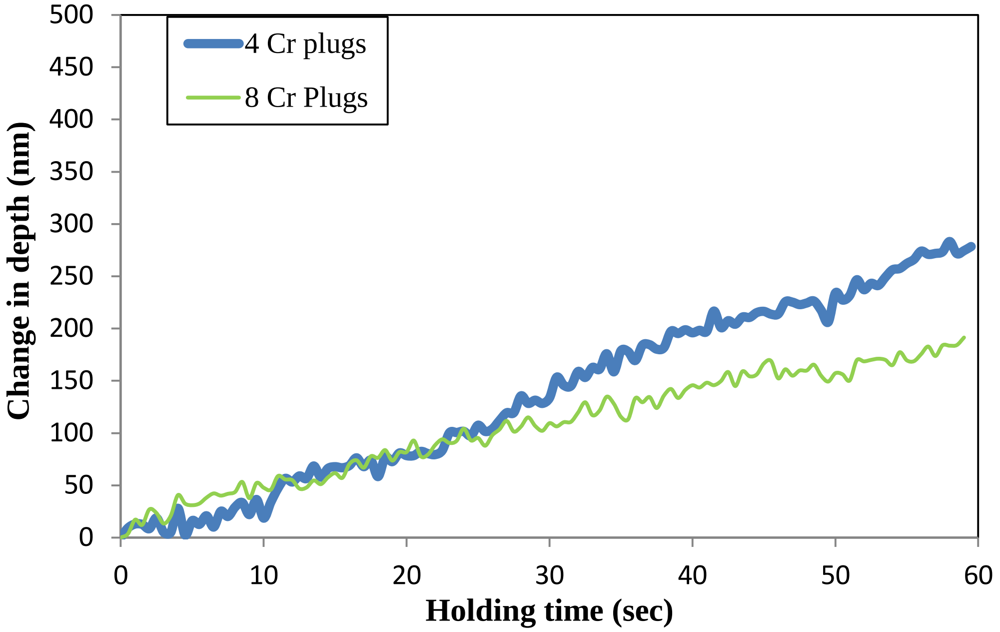

Figure 4-25 Variation in the penetration depth with load-holding time at 50 ^{o}C by 20 mN load.

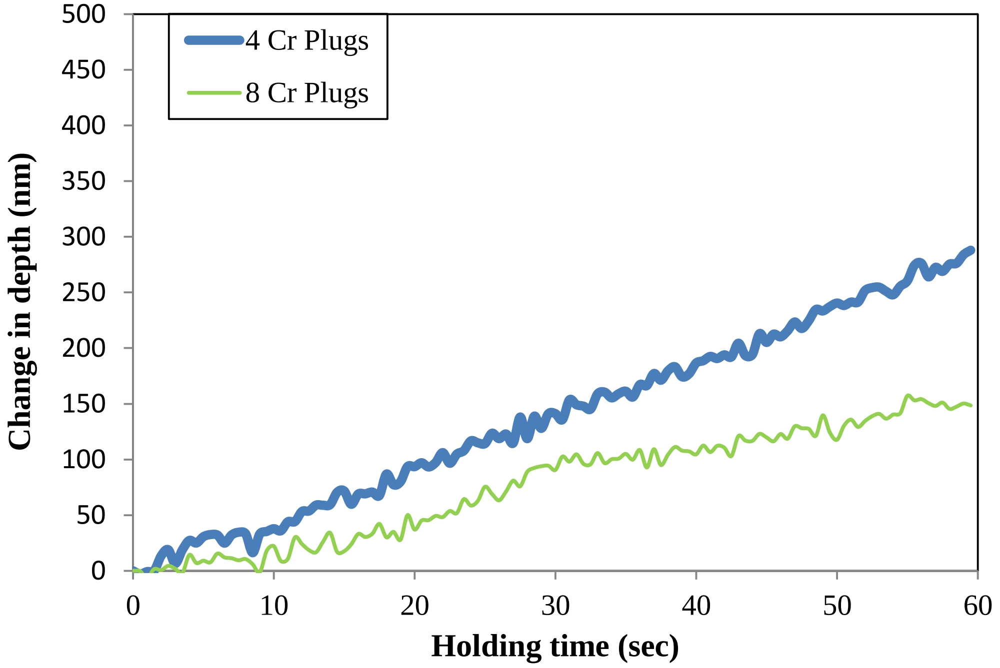

Figure 4-26 Variation in the penetration depth with load-holding time at 50 ^{o}C by 40 mN load.

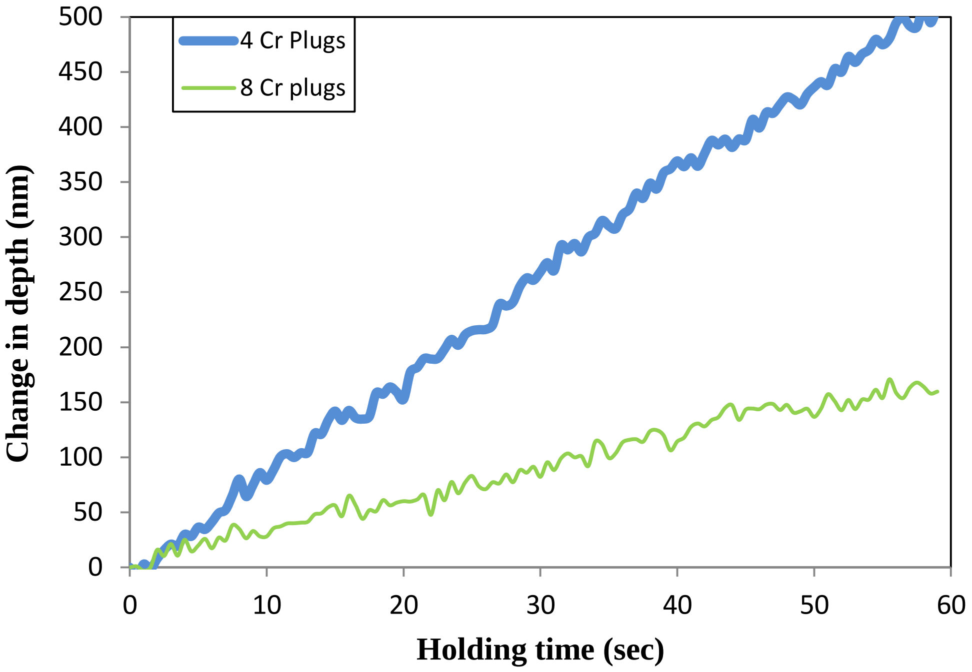

Figure 4-27 Variation in the penetration depth with load-holding time at 50 ^{o}C by 60 mN load.

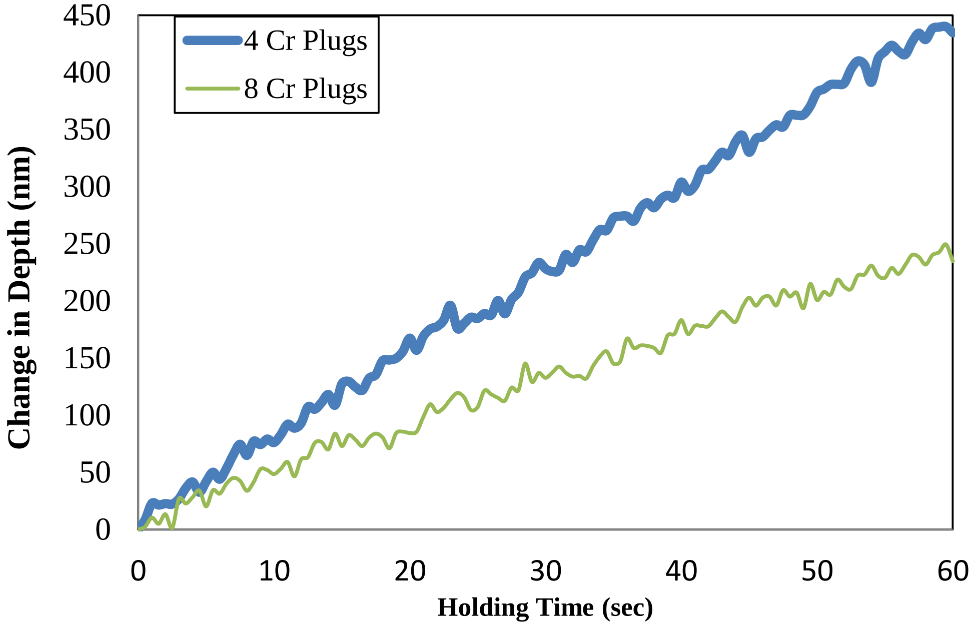

Figure 4-28 Variation in the penetration depth with load-holding time at 75 ^{o}C by 20 mN load.

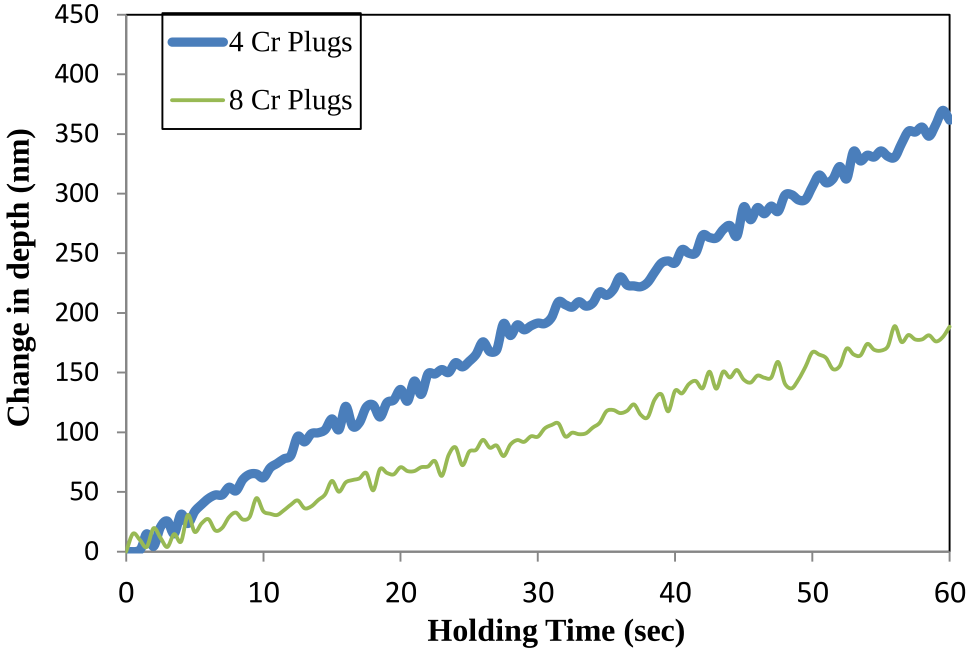

Figure 4-29 Variation in the penetration depth with load-holding time at 75 ^{o}C by 40 mN load.

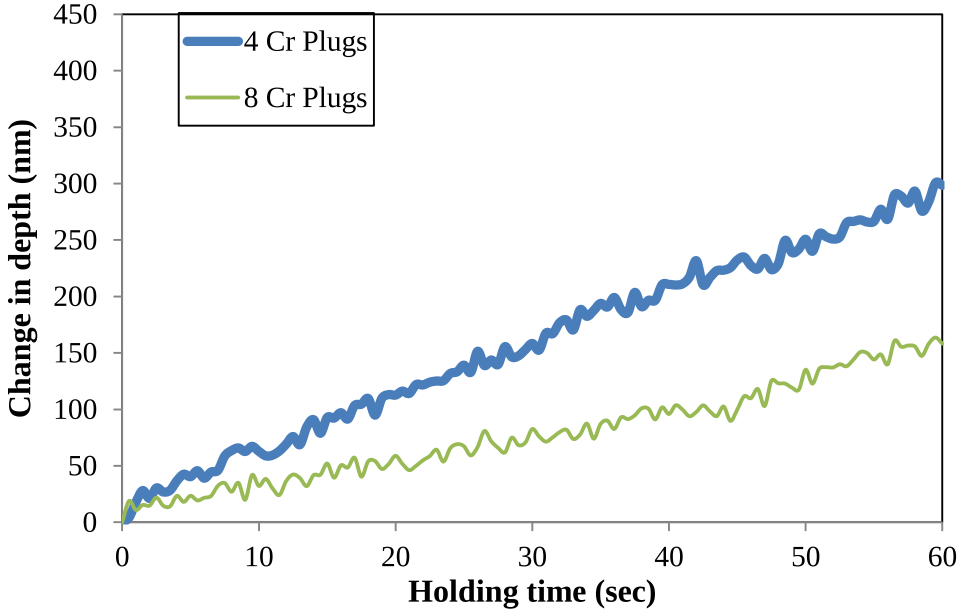

Figure 4-30 Variation in the penetration depth with load-holding time at 75 ^{o}C by 60 mN load.

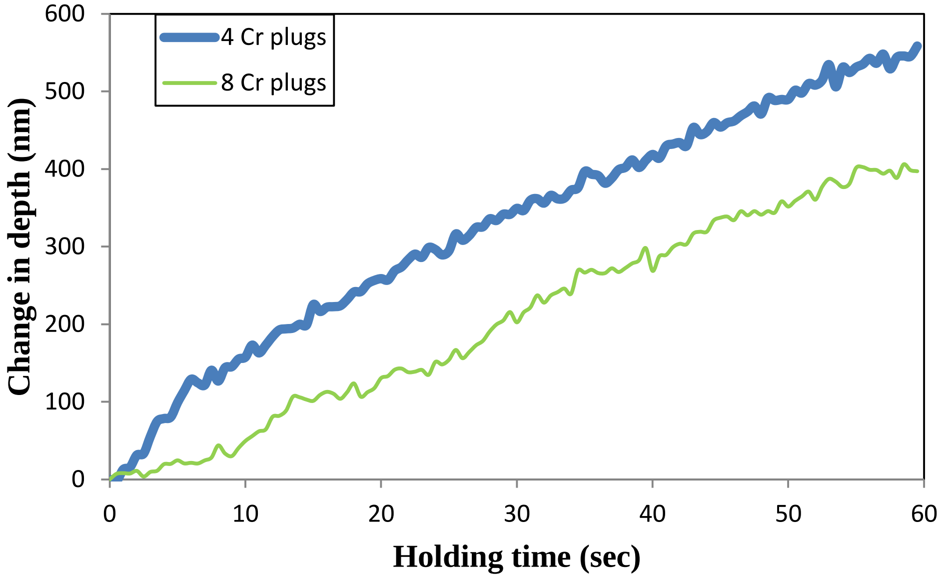

Figure 4-31 Variation in the penetration depth with load-holding time at 100 ^{o}C by 20 mN load.

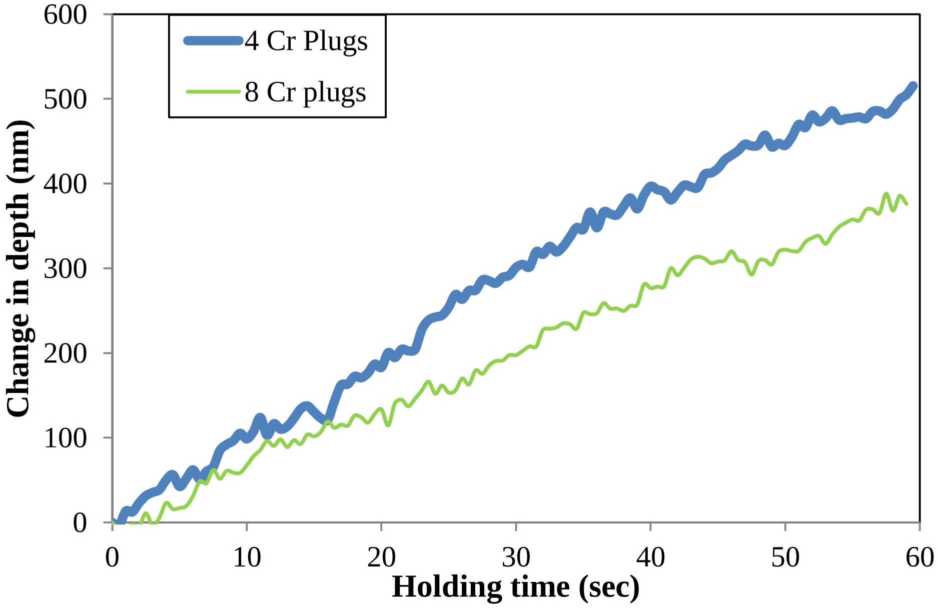

Figure 4-32 Variation in the penetration depth with load-holding time at 100 ^{o}C by 40 mN load.

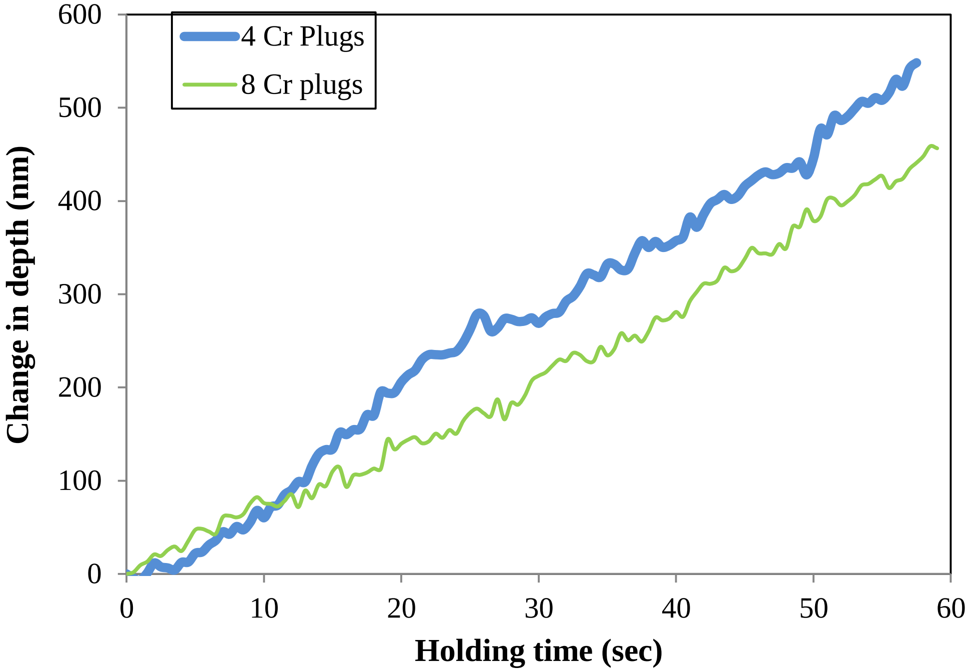

Figure 4-33 Variation in the penetration depth with load-holding time at 100 ^{o}C by 60 mN load.

Table 4-8 Creep rate (nm/sec) of coatings deposited by target 1 and target 2 at different temperatures.

Temperature (^oC)	Load (mN)	Creep Rate (nm/sec)	
		Target 1 (8 Cr plugs)	Target 2 (4 Cr plugs)
50	20	2.9	4.9
	40	2.8	4.8
	60	2.8	8.8
75	20	3.9	7.3
	40	3.1	5.9
	60	2.4	4.7
100	20	7.4	8.6
	40	6.6	8.6
	60	7.7	9.5

4.4 Wear

Wear analysis was done with alumina hard ball (dia. 1.5mm) with 10 N normal load. Table 4-9 shows the wear rate for coating deposited using target 1 and target 2 at different biasing voltages. Apparently wear rate for coating deposited by target 1decreased with increasing biasing voltage. Highest wear rate was obtained for -30 V biased coating sample.

Table 4-9 Calculated wear rate of the coating samples against alumina hard ball.

Target	Biasing Voltage (V)	Wear Rate (gm/N-m)
Target 1 (8 Cr plugs)	-30	1.09×10^{-5}
	-50	0.63×10^{-5}
	-60	0.47×10^{-5}
Target 2 (4 Cr plugs)	-50	0.58×10^{-5}

CHAPTER 5

DISCUSSION

5.1 Scratch Resistance

5.1.1. Effect of Biasing Voltage

As it clear from Table 4-7 that hardness of the coatings increased with increasing biasing voltage. Other characteristics such as surface grain size, composition and phases present are similar in each biasing voltage of target 1 coating. One of the reasons for increase in hardness value with biasing voltage is higher residual stresses developed during deposition process. As biasing voltage was increased, energy of ejecting atoms also increased. This increase in ejecting atom's energy could be responsible for the increase in residual stresses. This is also verified from table provided by Le Bourhis et al [26] (Table 2-1) that residual stress increased with hardness of the coating in most of the analysis.

The critical load (L_c) at which coating starts to fail corresponds to a sudden increase in the AE amplitude. There are various parameters which affect the critical load like, scratching velocity, stylus properties, etc. and coating-substrate composite properties like hardness and surface roughness [46, 47]. The generated AE signals showed various spikes in -60 V biased sample as compared to -30 V biased sample. This might be attributed to the high energy release in -60 V biased sample due to higher residual stresses developed during coating process. Increase in residual stresses increases the brittleness of the coating. Apparently coating failure was cohesive in both coating samples because the behavior of AE signal is the same throughout the scratch track. The critical load for coating deposited using target 1 is almost the same at all biasing voltages. This indicates that critical load (L_c) is not sensitive to the level of target bias. However, the high residual stresses could have caused the large trackside delamination (shown in Figure 5-6). Coating delamination in -60 V biased sample is away from the trackside whereas in -30 V biased it is near the trackside. High trackside delamination in -60 V biased is also visible from panorama view shown in Figure 4-8 and Figure 4-9. High trackside delamination might be due to relaxation of residual stresses and because of the difference in elastic properties of the substrate and the coating. At certain load substrate starts to deform plastically while coating was hard to deform plastically with the substrate. This creates the shear stress across the coating thickness due to normal force. This shear stress causes the failure of the coating with delamination. Coating having high residual stress causes delamination away from the scratch track.

The coating failure mode is a complex phenomenon and generally more than one mode can exist in a single coating [48]. Cracking mode depends on the type of stress causing coating failure. Indenter exerts a tensile force at the rear end and compressive force at the front edge of the coating. Schematic of developed tensile cracks and conformal cracks are shown in Figure 5-1 and Figure 5-2, respectively. Coating failure due to tensile stress at the rear end causes the semi-circular cracks opening towards the indenter motion are termed as tensile or forward cracking. Coating failure due to compressive stress at the front edge of the indenter generates semi-circular cracks opening opposite of the indenter motion is termed as conformal or compressive cracks [49]. It is also found that coatings fail in several different ways when subjected to scratch testing [50, 51]. Figure 5-3, Figure 5-4 and Figure 5-5 show the cracking mode for -30 V, -50 V and -60 V biased samples, deposited using target 1, respectively. As shown in Figure 5-3, -30 V biased sample the cracking mode appears dominated by tensile cracking. Coating spallation (Buckling) was also observed. The spalling coating failure occurred due to compressive stress field in front of the moving indenter. Coating biased at -50 V and -60 V were dominated by conformal cracking mode. Due to high residual stresses, cracks developed by the indenter propagated along the interface and away from the track which resulted in large buckling of the coating. Tensile cracks in -30 V biased coating and conformal cracks in -50 V and -60 V biased coatings indicate that higher biased coatings are more brittle than lower biased coating. Part of the coating was present in the scratch track. The developed cracks were close to the leading edge of the indenter that's why chip of the coating was embedded in the bottom of the track.

5.1.2. Effect of Cr/Al Ratio

Scratch panorama and its corresponding AE signal for coating depositing using target 2 (-50 V biasing) is shown in Figure 4-16. In target 2 coating AE signal increased up to a constant value. This may be the result of more than one failure mode along the scratch track. This behavior could be related to the influence of the substrate. Failure started as a cohesive failure and with increasing substrate influence adhesive failure occurred. Complete adhesive failure started at around 7 N which continued up to the end. Figure 5-7 shows the coating failure mode in coating deposited using target 2, biased at -50 V. The failure mode in target 2 coating was predominated by tensile cracking mode [49]. Cracks have been generated by the tensile stresses at the trailing edge of the indenter.

There was no visible trackside delamination. This type of coating failure mode indicated that target 2 coating sample is ductile. However, coating deposited using target 1, -50 V biased, showed conformal cracks with large trackside delamination. No trackside delamination in coating deposited by target 2, -50 V biased, might be because of lower hardness value of the coating but enough hardness to resist the penetration of the indenter. Due to low hardness coating deformed plastically with substrate. This caused the indenter move over the coating instead of spallation or buckling. This indicates that large difference in substrate and coating hardness value causes the coating spallation. Branching like coating spallation in -50 V and -60 V (target 1) biased coating samples also support the explanation.

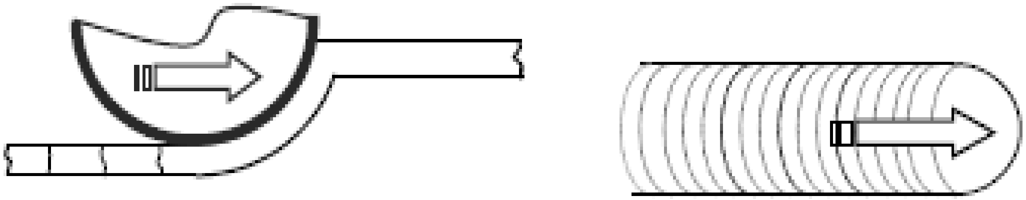

Figure 5-1 Schematic of generated tensile cracks due tensile stress at the rear end of indenter [49].

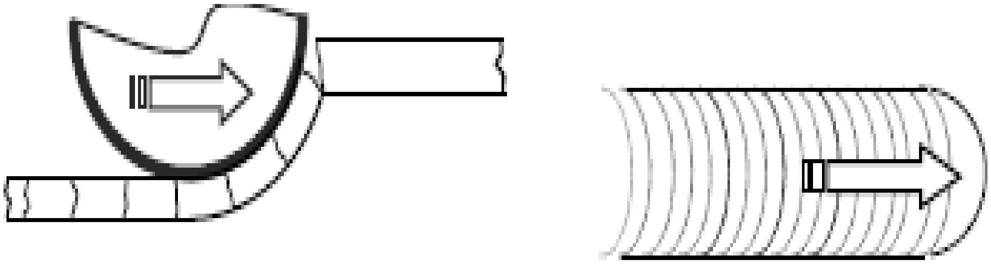

Figure 5-2 Schematic of developed conformal cracks generated due to compressive stresses at the front of indenter [49].

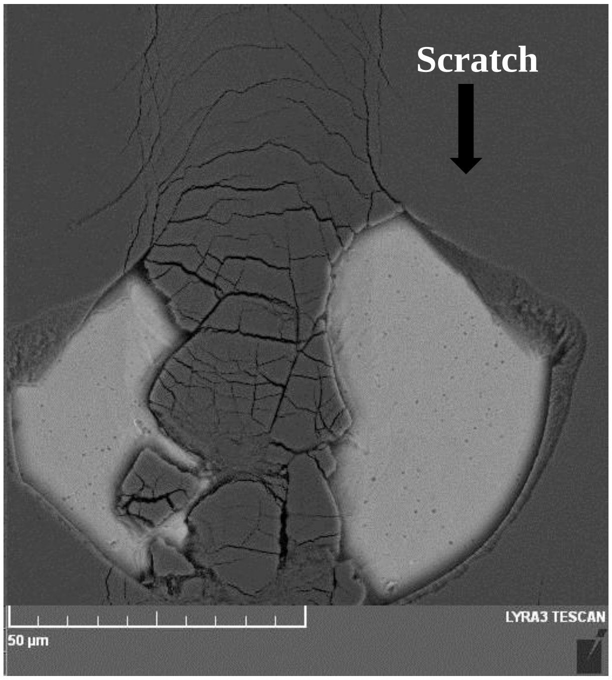

Figure 5-3 Field Emission SEM micrograph showing tensile cracks and crack side delamination of coating deposited using target 1 at -30 V biasing.

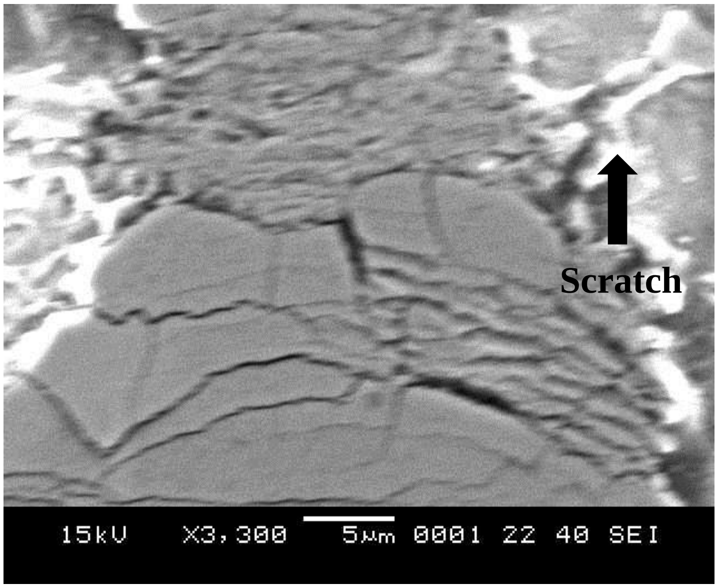

Figure 5-4 Field Emission SEM micrograph showing conformal cracks and track side delamination of coating deposited using target 1 biased at-50 V.

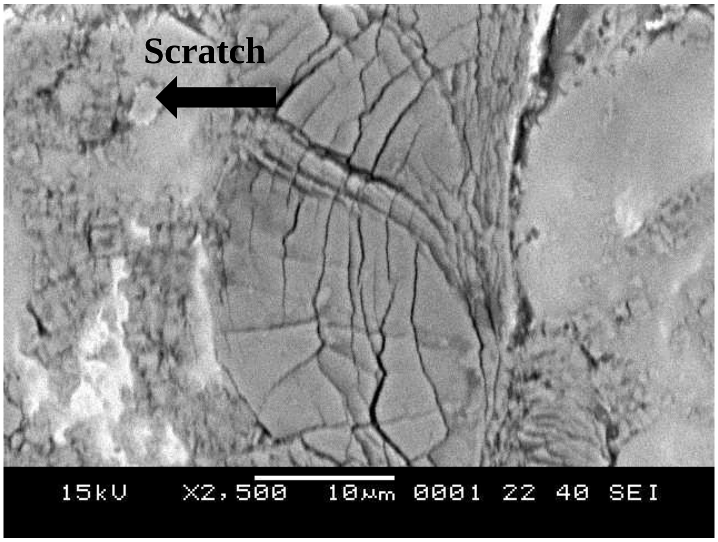

Figure 5-5 Field Emission SEM micrograph showing conformal cracks and track side delamination of the coating deposited using target 1 biased at-60 V.

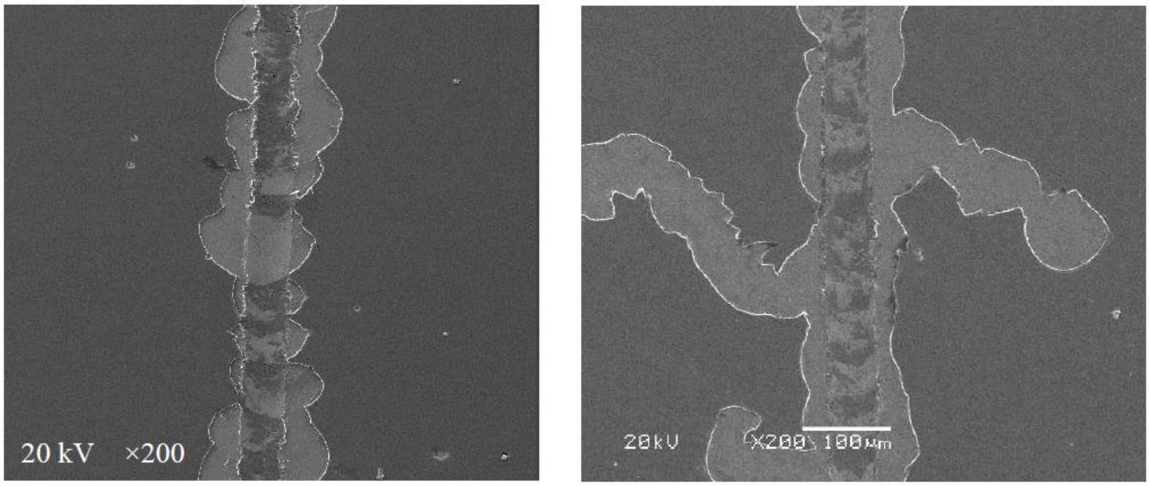

(a) (b)

Figure 5-6 Field Emission SEM micrographs of coating deposited using target 1 at (a) -30 V and (b) -60 V showing track side delamination.

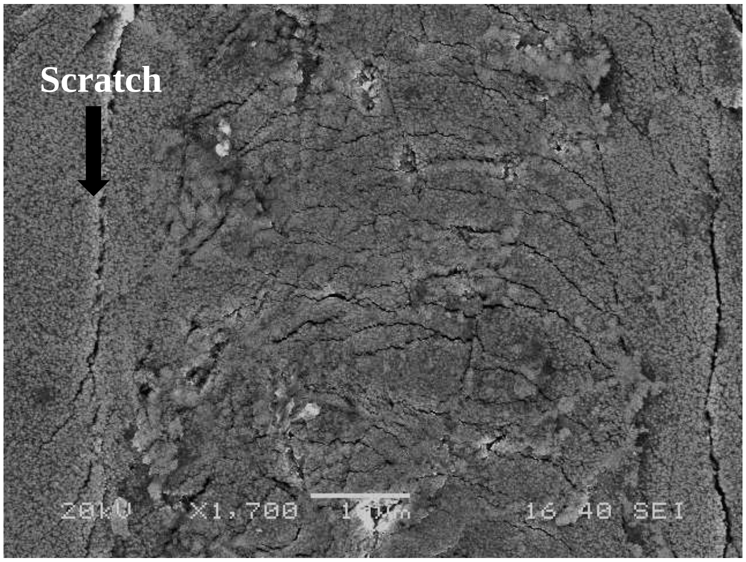

Figure 5-7 Field Emission SEM micrograph showing tensile cracks of coating deposited using target 2 at -50 V biased.

5.2 Creep Resistance

5.2.1. Effect of Cr/Al ratio

In this present study coatings with high Cr/Al content and low Cr/Al content were investigated. High Cr/Al content coating was harder than lower Cr/Al content coating. In high Cr/Al content coating one cubic phase of AlCrN existed while low Cr/Al content coating contained cubic phase of AlCrN with hexagonal phase Cr_2N. At room temperature creep was observed only in lower Cr/Al content coating. There was no creep in high Cr/Al content coating. This indicated that creep resistance was higher for higher Cr/Al content coating at room temperature. One of the reasons causing high creep resistance for high Cr/Al content might be due to high hardness value. It has been reported that indentation creep depth decreases with increasing hardness value [52]. Also lower Cr/Al content coating contained mixed phases. This might be also the reason for higher penetration rate in low Cr/Al content coating. At 50 ^{o}C and 75 ^{o}C, creep occurred in both coatings. Apparently creep curve was linear in nature (Figure 4-25 to Figure 4-30). This indicated that penetration rate was constant for the duration of holding time. Penetration rates for high Cr/Al content and low Cr/Al content coatings at 20 mN and 40 mN over the range of temperature 25 ^{o}C to 75 ^{o}C are shown in Figure 5-8 and Figure 5-9 respectively. It is clear from the figures that penetration rate decreased with increasing temperature. Penetration rates were not significantly affected by the applied load. It has been reported that creep resistance is independent of applied load [42]. At 75 ^{o}C and 100 ^{o}C with 60 mN load indenter penetration was around 40 % and 60 % of the coating thickness, respectively. At high indenter penetration creep was possibly affected by the substrate. As load and temperature were increased indenter penetration also increased. The substrate interference can be also verified from the penetration rates at 100 ^{o}C. Penetration rates of both the coatings approached similar values. These reasons have invalidated the penetration rates at higher temperature with 60 mN load.

The activation energy (Q) was calculated by assuming that penetration rate was proportional to exp(-Q/RT) according to equation (4).

$$\dot{\varepsilon} \propto \exp(-\frac{Q}{RT}) \qquad \text{…..(4)}$$

Where R is the gas constant and T is the temperature in kelvin. The calculated activation energies were 19305.7 J/mol and 12297.1 J/mol for high Cr/Al content and low Cr/Al content coatings, respectively. The calculated activation energies are consistent with the results indicating high creep resistance for high Cr/Al content coating.

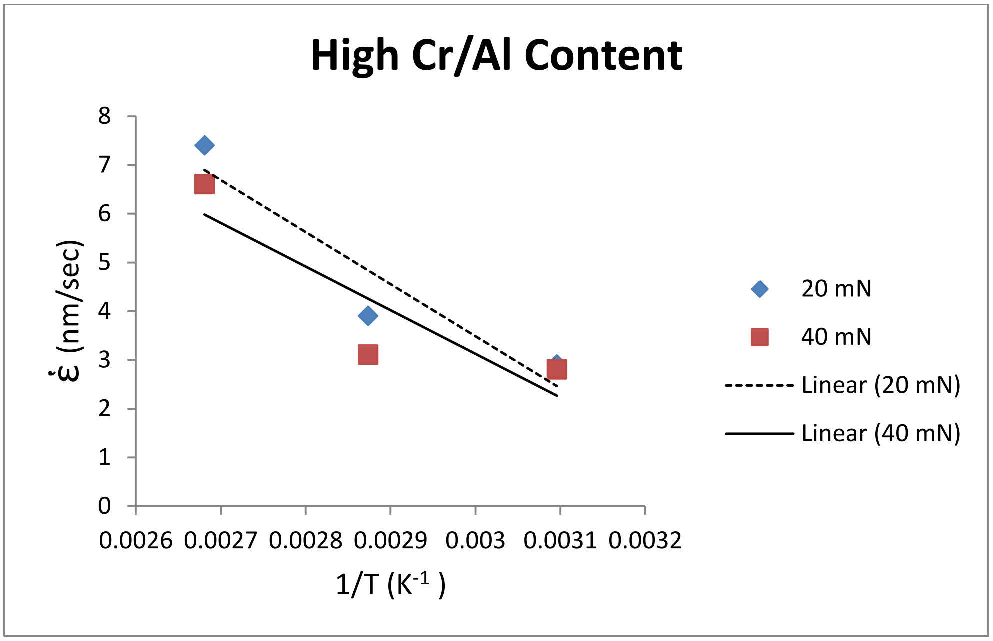

Figure 5-8 Penetration rates of high Cr/Al content coating at 20 mN and 40 mN load.

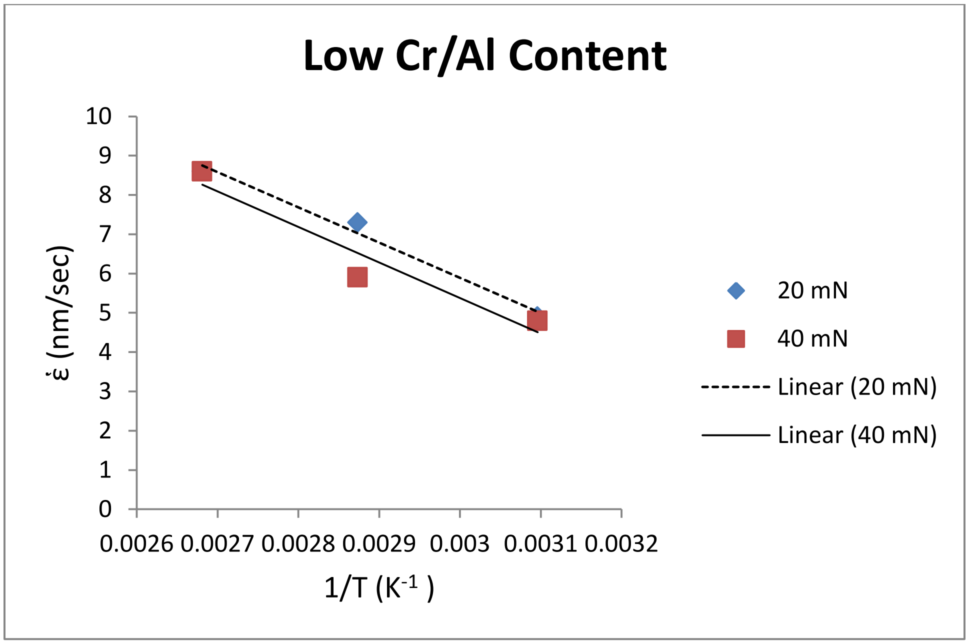

Figure 5-9 Penetration rates of low Cr/Al content coating at 20 mN and 40 mN load.

5.3 Wear Resistance

Wear rate of the coatings are shown in Table 4-9. It was observed during scratch test analysis that coating deposited at high negative biasing voltage has high trackside delamination due to residual stresses. On the basis of these observations wear rate was expected higher for higher biasing voltage but our results were contrary to this hypothesis. The reason behind this may be that scratch test was performed by sharp edged indenter whereas in wear test a spherical ball was used. The sharp edged (100 µm dia.) created a higher stress than the ball (1.5 mm dia.). Hardness of the coating obtained higher for higher biasing voltage. Increasing hardness with biasing voltage might be one of the reasons controlling the wear rate. Wear rate was higher in -30 V biased sample because of lower hardness value. Wear rate for high and low Cr/Al content coatings (fixed biasing voltage -50 V) were close to each other while higher Cr/Al content coating was higher in hardness. This might be due to coating delamination resistance of lower Cr/Al coating. Figure 5-10 and Figure 5-11 show trackside delamination of coatings deposited using 8 Cr plugs (high Cr/Al content) and 4 Cr plugs (low Cr/Al content), respectively. It is evident from the figures that there is no coating delamination in low Cr/Al content coating. No coating delamination in lower Cr/Al content coating could be the dominant factor controlling the wear rate.

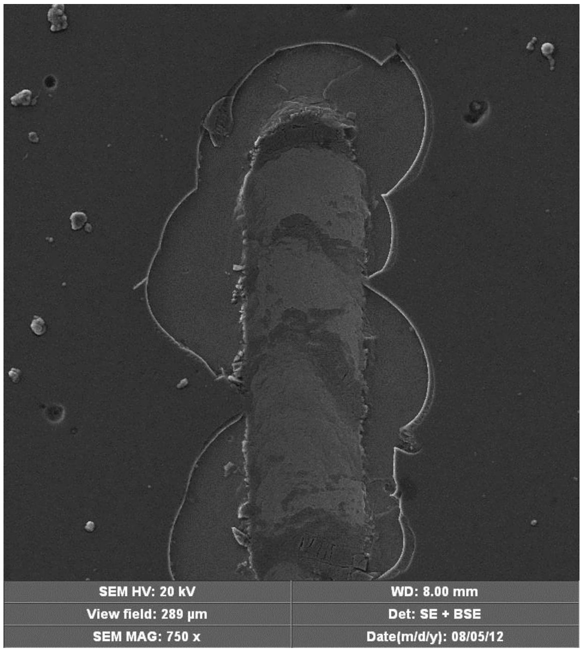

Figure 5-10 SEM micrograph showing trackside delamination in coating deposited using 8 Cr plugs biased at -50 V.

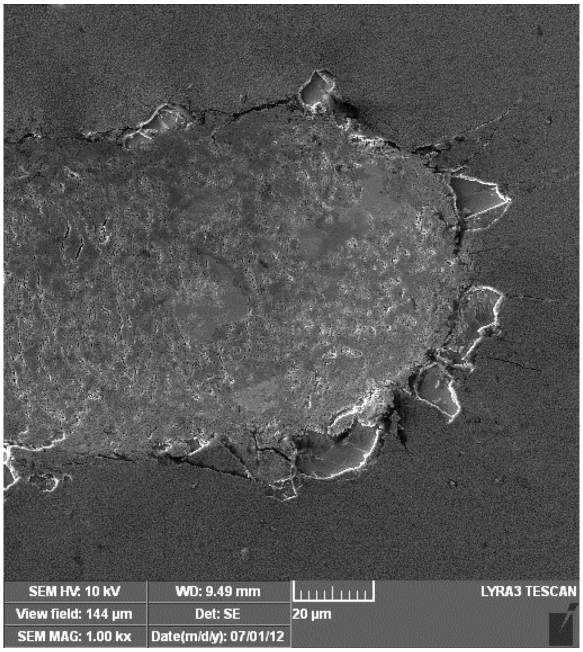

Figure 5-11 SEM micrograph showing trackside delamination in coating deposited using 4 Cr plugs biased at -50 V.

CHAPTER 6

CONCLUSION

The overall objective of this work was to evaluate the effects of biasing voltages (-30V, -50V, -60V) and Cr/Al content on the scratch resistance, creep resistance and wear resistance of the AlCrN coatings. The following are the key conclusions:

1. The surface morphology of magnetron sputtered AlCrN coating deposited using 4 Cr plugs was coarser than 8 Cr plugs coating. This indicated that surface grains became finer with increasing Cr/Al ratio.
2. Coatings deposited in this study consisted of multiple layers with varying compositions.
3. The coating containing higher Cr/Al content showed only one phase of cubic AlCr-N while lower Cr/Al content coating showed mixed phases of cubic AlCr-N and hexagonal Cr_2N.
4. The higher Cr/Al content coatings showed high hardness values. The highest hardness was obtained for coating deposited using 8 Cr plugs target at -60 V biasing.
5. Scratch resistance in terms of the critical load (L_c) was found higher for higher Cr/Al content coating. The critical load (L_c) seemed independent of biasing voltage.
6. The higher Cr/Al content coating showed large trackside delamination. The trackside delamination increased with increasing biasing voltage.

7. The creep resistance of the coating was dependent on the Cr/Al ratio. Higher creep resistance was found for higher Cr/Al content coating over the range of 25 ^{o}C to 75 ^{o}C.
8. Wear resistance for higher Cr/Al content coating, tested against alumina ball, increased with increasing biasing voltage.
9. Wear rate of low and high Cr/Al content coatings at fixed biasing voltage of -50 V were essentially similar. This is possibly because of no trackside delamination in low Cr/Al content coating.

References

[1] R.J. Rodríguez, J.A. García, A. Medrano, M. Rico, R. Sánchez, R. Martínez, C. Labrugère, M. Lahaye, A. Guette, Vacuum, 67 (2002) 559-566.

[2] J.V. Ramana, S. Kumar, C. David, V.S. Raju, Materials Letters, 58 (2004) 2553-2558.

[3] O. Banakh, P.E. Schmid, R. Sanjinés, F. Lévy, Surface and Coatings Technology, 163–164 (2003) 57-61.

[4] R. Lamni, R. Sanjinés, F. Lévy, Thin Solid Films, 478 (2005) 170-175.

[5] M. Arndt, T. Kacsich, Surface and Coatings Technology, 163–164 (2003) 674-680.

[6] J.L. Endrino, G.S. Fox-Rabinovich, C. Gey, Surface and Coatings Technology, 200 (2006) 6840-6845.

[7] P.S. McLeod, L.D. Hartsough, Journal of Vacuum Science and Technology, 14 (1977) 263-265.

[8] B. Window, N. Savvides, Journal of Vacuum Science & Technology A: Vacuum, Surfaces, and Films, 4 (1986) 196-202.

[9] P.J. Kelly, R.D. Arnell, Vacuum, 56 (2000) 159-172.

[10] J. Danroc, A. Aubert, R. Gillet, Surface and Coatings Technology, 33 (1987) 83-90.

[11] J.P. Lehan, R.B. Sargent, R.E. Klinger, Journal of Vacuum Science & Technology A: Vacuum, Surfaces, and Films, 10 (1992) 3401-3406.

[12] C.D. Tsiogas, J.N. Avaritsiotis, Vacuum, 43 (1992) 203-211.

[13] P. Losbichler, C. Mitterer, W.S.M. Werner, H. Störi, J. Barounig, Thin Solid Films, 228 (1993) 56-59.

[14] A. Schröer, W. Ensinger, G.K. Wolf, Materials Science and Engineering: A, 140 (1991) 625-630.

[15] M. Stüber, V. Schier, H. Holleck, Surface and Coatings Technology, 74–75 Part 2 (1995) 833-837.

[16] R. Manaila, D. Biro, A. Devenyi, D. Fratiloiu, R. Popescu, J.E. Totolici, Applied Surface Science, 134 (1998) 1-10.

[17] L. Cunha, M. Andritschky, L. Rebouta, R. Silva, Thin Solid Films, 317 (1998) 351-355.

[18] A. Lousa, J. Esteve, S. Muhl, Mart, E. nez, Diamond and Related Materials, 9 (2000) 502-505.

[19] T. Berlind, N. Hellgren, M.P. Johansson, L. Hultman, Surface and Coatings Technology, 141 (2001) 145-155.

[20] D. Song, Applied Surface Science, 254 (2008) 4171-4178.

[21] J. Musil, P. Baroch, Vacuum, 87 (2013) 96-102.

[22] K. Singh, P.K. Limaye, N.L. Soni, A.K. Grover, R.G. Agrawal, A.K. Suri, Wear, 258 (2005) 1813-1824.

[23] J. Deng, J. Liu, J. Zhao, W. Song, International Journal of Refractory Metals and Hard Materials, 26 (2008) 164-172.

[24] V.R. Parameswaran, J.P. Immarigeon, D. Nagy, Surface and Coatings Technology, 52 (1992) 251-260.

[25] X.T. Zeng, S. Zhang, C.Q. Sun, Y.C. Liu, Thin Solid Films, 424 (2003) 99-102.

[26] E. Le Bourhis, P. Goudeau, M.H. Staia, E. Carrasquero, E.S. Puchi-Cabrera, Surface and Coatings Technology, 203 (2009) 2961-2968.

[27] R. Hoy, W.G. Sloof, G.C.A.M. Janssen, Surface and Coatings Technology, 179 (2004) 215-222.
[28] A.E. Reiter, V.H. Derflinger, B. Hanselmann, T. Bachmann, B. Sartory, Surface and Coatings Technology, 200 (2005) 2114-2122.
[29] G.S. Kim, S.Y. Lee, Surface and Coatings Technology, 201 (2006) 4361-4366.
[30] G.S. Fox-Rabinovich, B.D. Beake, J.L. Endrino, S.C. Veldhuis, R. Parkinson, L.S. Shuster, M.S. Migranov, Surface and Coatings Technology, 200 (2006) 5738-5742.
[31] Y.-J. Lin, A. Agrawal, Y. Fang, Wear, 264 (2008) 226-234.
[32] J. Lin, B. Mishra, J.J. Moore, W.D. Sproul, Surface and Coatings Technology, 202 (2008) 3272-3283.
[33] C. Brecher, G. Spachtholz, K. Bobzin, E. Lugscheider, O. Knotek, M. Maes, Surface and Coatings Technology, 200 (2005) 1738-1744.
[34] X.-Z. Ding, X.T. Zeng, Surface and Coatings Technology, 200 (2005) 1372-1376.
[35] X.-z. Ding, X.T. Zeng, Y.C. Liu, F.Z. Fang, G.C. Lim, Thin Solid Films, 516 (2008) 1710-1715.
[36] J.L. Mo, M.H. Zhu, Tribology International, 41 (2008) 1161-1168.
[37] R.A. Surmenev, Surface and Coatings Technology, 206 (2012) 2035-2056.
[38] S. Wen, F. Zeng, Y. Gao, F. Pan, Scripta Materialia, 55 (2006) 187-190.
[39] T.W. Wu, M. Moshref, P.S. Alexopoulos, Thin Solid Films, 187 (1990) 295-307.
[40] M. Mayo, W. Nix, Acta Metallurgica, 36 (1988) 2183-2192.
[41] V. Raman, R. Berriche, J. Mater. Res, 7 (1992) 627-638.
[42] T. Chudoba, F. Richter, Surface and Coatings Technology, 148 (2001) 191-198.
[43] W. Yan, N.P. O'Dowd, E.P. Busso, Journal of the Mechanics and Physics of Solids, 50 (2002) 449-470.
[44] J. Lin, J.J. Moore, J. Wang, W.D. Sproul, Thin Solid Films, 519 (2011) 2402-2408.
[45] T. Polcar, A. Cavaleiro, Materials Chemistry and Physics, 129 (2011) 195-201.
[46] P.A. Steinmann, Y. Tardy, H.E. Hintermann, Thin Solid Films, 154 (1987) 333-349.
[47] J. Valli, U. Mäkelä, Wear, 115 (1987) 215-221.
[48] S.J. Bull, Tribology International, 30 (1997) 491-498.
[49] P.J. Burnett, D.S. Rickerby, Thin Solid Films, 154 (1987) 403-416.
[50] S.J. Bull, D.S. Rickerby, A. Matthews, A. Leyland, A.R. Pace, J. Valli, Surface and Coatings Technology, 36 (1988) 503-517.
[51] S.J. Bull, Surface and Coatings Technology, 50 (1991) 25-32.
[52] S.P. Wen, F. Zeng, Y. Gao, F. Pan, Scripta Materialia, 55 (2006) 187-190.
[53] W.B. Li, R. Warren, Acta Metallurgica et Materialia, 41 (1993) 3065-3069.

Vitae

Name : Shahnawaz Alam

Nationality : Indian

Date of Birth :3/1/1987

Email : shaikhuamu@gmail.com

Address :Varanasi, Uttar Pradesh (India)

Academic Background : *Bachelor of Technology* in Mechnical Engineering; June 2010

Zakir Hussain College of Engineering & Technology (ZHCET)

Aligarh Muslim University (AMU) Aligarh, INDIA

Master of Science in Material and Manufacturing Engineering (Mechanical Engineering); April 2013

King Fahd University of Petroleum & Minerals (KFUPM)

Dhahran

Research Interests : Tribological Behavior, Hard Coatings, Corrosion

Email : shaikhuamu@gmail.com